

# 1 Atmospheric CO<sub>2</sub> dynamics in a coastal megacity: spatiotemporal 2 patterns, sea–land breeze impacts, and anthropogenic–biogenic 3 emission partitioning

4 Jinwen Zhang<sup>1</sup>, Yongjian Liang<sup>2</sup>, Chenglei Pei<sup>2</sup>, Bo Huang<sup>3</sup>, Yingyan Huang<sup>2</sup>, Xiufeng Lian<sup>1,3</sup>,  
5 Shaojie Song<sup>4</sup>, Chunlei Cheng<sup>1</sup>, Cheng Wu<sup>1</sup>, Zhen Zhou<sup>1</sup>, Junjie Li<sup>5</sup>, Mei Li<sup>1\*</sup>

6 <sup>1</sup>College of Environment and Climate, Institute of Mass Spectrometry and Atmospheric Environment, Guangdong  
7 Provincial Engineering Research Center for Online Source Apportionment System of Air Pollution, Guangdong–  
8 Hongkong–Macau Joint Laboratory of Collaborative Innovation for Environmental Quality, Jinan University,  
9 Guangzhou 511443, China

10 <sup>2</sup>Guangzhou Ecological and Environmental Monitoring Center Station, Guangdong, Guangzhou 510006, China

11 <sup>3</sup>Guangzhou Hexin Instrument Co., Ltd., Guangdong, Guangzhou 510530, China

12 <sup>4</sup>College of Environmental Science and Engineering, Nankai University, Tianjin 300350, China

13 <sup>5</sup>School of Environment, Beijing Jiaotong University, Beijing 100044, China

14 *Correspondence to:* Mei Li (limei@jnu.edu.cn)

15 **Abstract.** Attributing observed carbon dioxide (CO<sub>2</sub>) to fossil-fuel emissions versus biogenic fluxes is essential  
16 for assessing urban mitigation, but in coastal megacities it is complicated by anthropogenic–biogenic coupling and  
17 sea–land breeze (SLB) circulation. Here we analyze Guangzhou using multi-site in situ CO<sub>2</sub> and CO measurements  
18 (January 2023–September 2024), transport footprints, and a site-specific  $\Delta\text{CO}/\Delta\text{CO}_2$  ( $R_{\text{CO}}$ ) relationship to resolve  
19 spatiotemporal variability, quantify SLB effects, and partition fossil-fuel (CO<sub>2</sub>ff) and biogenic (CO<sub>2</sub>bio)  
20 contributions without assimilating emission inventories. Along a coastal–urban–suburban gradient, the coastal site  
21 shows the largest seasonal amplitude (~~25.63 ppm~~), the vegetated site exhibits strong summertime diurnal amplitude  
22 (~~39.90 ppm~~), and the urban core is combustion-dominated. **These gradients reveal a “coastal CO<sub>2</sub> dome” that—**  
23 **unlike urban domes often conceptualized as core-anchored—is seasonally displaced, with peak concentrations**  
24 **shifting away from the core due to the interplay of coastal ventilation and biogenic exchange.** SLB effects are  
25 seasonal: SLB ventilates CO<sub>2</sub> in spring–winter but promotes summertime accumulation (+2.08 ppm) under stable  
26 stratification, accompanied by pronounced CO enhancements, consistent with trapped/recirculated combustion  
27 plumes. Regression-derived urban  $R_{\text{CO}}$  is consistent with ~~reported~~ post-2013 broad tightening of coal/industrial and  
28 vehicle-emission controls. Winter-afternoon urban CO<sub>2</sub>ff attribution remains robust to transport-model  
29 configurations and ~~quantified~~ measurement/background uncertainty. Summer-afternoon CO<sub>2</sub>bio **shows substantial**  
30 **biogenic uptake is  $-3.59 \pm 0.63 \mu\text{mol m}^{-2} \text{s}^{-1}$** , offsetting ~~up to~~  $\sim 60\%$  of concurrent CO<sub>2</sub>ff. These results  
31 demonstrate that coastal dynamics and urban greening reshape observed CO<sub>2</sub> signals, highlighting that biogenic–  
32 anthropogenic decoupling and SLB-aware sampling are essential for the robust evaluation of carbon mitigation in

33 coastal megacities.

## 34 **1 Introduction**

35 Atmospheric carbon dioxide (CO<sub>2</sub>), the predominant anthropogenic driver of climate change, is accumulating at  
36 unprecedented rates in human history (WMO, 2024). Future CO<sub>2</sub> increments will exert stronger warming effects  
37 than equivalent past increases due to climate system feedbacks (He et al., 2023), making emission control  
38 imperative. Despite covering only 3 % of global land, urban areas generate over 70 % of carbon emissions (Crippa  
39 et al., 2021), positioning cities as critical arenas where mitigation policies, infrastructure transitions, and urban  
40 greening can drive measurable changes in urban carbon budgets (WMO, 2025).

41

42 Urban atmospheric CO<sub>2</sub> concentrations provide a complementary constraint to flux- or inventory-based  
43 assessments because they integrate surface emissions, biogenic exchange, and atmospheric transport over the  
44 upwind source area (Lin et al., 2003; Shusterman et al., 2018; Pitt et al., 2022). This integration, however, creates  
45 an attribution challenge because observed CO<sub>2</sub> variability reflects coupled effects of fossil-fuel emissions, biogenic  
46 fluxes, and meteorology/transport, and thus is not uniquely attributable to any single driver, although one factor  
47 may dominate in certain regimes, especially on diurnal to seasonal timescales (Xueref-Remy et al., 2018; Yang et  
48 al., 2021; Mitchell et al., 2018). The challenge is particularly acute in coastal megacities, where land–sea thermal  
49 contrasts and marine background inflow drive strong diurnal reversals in advection and boundary-layer structure  
50 (Leroyer et al., 2014; Lei et al., 2024). These dynamics complicate observational representativeness and source–  
51 sink separation, and can make inferred CO<sub>2</sub> enhancements sensitive to background selection under different  
52 transport regimes (Verhulst et al., 2017). Given their high exposure to climate-related hazards, especially flooding  
53 and storm impacts, coastal megacities are priority targets for climate-risk management, motivating robust, policy-  
54 relevant CO<sub>2</sub> emissions assessment (Kumar, 2021).

55

56 A range of approaches has been used to constrain urban carbon budgets, including bottom-up inventories, tower-  
57 based atmospheric observations, tracer/isotope measurements, and atmospheric inversions. Bottom-up inventories  
58 provide essential baselines, yet urban emissions remain uncertain and can differ across products because they  
59 depend on activity/emission-factor assumptions and proxy-based downscaling (Gately and Hutyra, 2017; Gurney  
60 et al., 2019). While radiocarbon (<sup>14</sup>C) measurements provide robust fossil-fuel/biogenic partitioning (Turnbull et  
61 al., 2015; Berhanu et al., 2017; Wang et al., 2022), their high cost and discontinuous sampling limit their  
62 applicability for long-term, high-frequency monitoring. Similarly, eddy covariance (EC) measurements quantify

63 net CO<sub>2</sub> fluxes within tower footprints (typically 1–2 km radius), yet the derived flux partitioning reflects only  
64 local-scale dynamics and cannot fully represent city-wide carbon exchange processes (Velasco et al., 2013; Menzer  
65 and Mcfadden, 2017; Wu et al., 2022b). Fully three-dimensional (3-D) atmospheric inversions can assimilate  
66 concentration data to estimate city-scale emissions and quantify posterior uncertainty when observation networks  
67 adequately constrain boundary inflow and key transport uncertainties (Lauvaux et al., 2016; Lian et al., 2023). Yet  
68 in practice, urban inversions are often limited by incomplete observational coverage, representativeness (sub-grid)  
69 errors, and transport biases (Boon et al., 2016; Deng et al., 2017; Ye et al., 2020; Che et al., 2022b). They can also  
70 remain sensitive to choices of background/boundary conditions and prior assumptions, including those related to  
71 biogenic fluxes, which can be large and temporally variable during the growing season (Turnbull et al., 2018; Nalini  
72 et al., 2022; Ye et al., 2020). These constraints motivate complementary observation-driven frameworks that  
73 emphasize process-level interpretation of concentration variability while explicitly tracking uncertainty sources.

74

75 A defining coastal process is the sea–land breeze (SLB), a common mesoscale circulation driven by land–sea  
76 thermal contrast (Shen et al., 2021). In the Pearl River Estuary (PRE), SLB occurrence shows pronounced  
77 seasonality and spatial dependence, with spring–autumn maxima reported in parts of the region (You and Chi-Hung  
78 Fung, 2019; Mai et al., 2024b). SLB produces a clear diurnal reversal between onshore and offshore flow and can  
79 modify boundary-layer structure and mixing depth (Wu et al., 2013; Lei et al., 2024), complicating the  
80 interpretation of urban CO<sub>2</sub> variability. By contrast, inland basins/valleys lack marine inflow–outflow and may be  
81 shaped by lake–land breeze circulations (Yang et al., 2022) or other topography-modulated flows that can shift  
82 background conditions and the footprint representativeness of urban observations (Mitchell et al., 2018; Wang et  
83 al., 2021). Beyond the PRE, China’s coastal basins exhibit distinct SLB seasonality (e.g., a summer maximum in  
84 the Bohai Rim, weak seasonality in the Yangtze River Delta, and an autumn maximum in the PRE) (Huang et al.,  
85 2025), likely driven by regional differences in large-scale wind fields and air–sea turbulent heat fluxes (Shen et al.,  
86 2024), and potentially modulated by coastline geometry and topographic constraints. Despite recognized impacts  
87 of SLB on air quality (Zhao et al., 2022; Wang et al., 2023; Zheng et al., 2024), only a few case studies have  
88 examined how SLB-driven recirculation of nocturnally respired CO<sub>2</sub> can perturb daytime coastal CO<sub>2</sub>  
89 measurements and may bias emission inversions (Ahmadov et al., 2007), and systematic quantification across  
90 coastal cities remains limited.

91

92 Urban greening reinforces the need for explicit source–sink separation because neglecting biogenic contributions  
93 can bias inferred urban emissions (Miller et al., 2020; Ye et al., 2020; Sargent et al., 2018). Moreover, urban

94 vegetation is often highly fragmented and can be underrepresented in moderate-to-coarse remote-sensing land-  
95 cover/canopy products, which may miss fine-scale urban heterogeneity and thereby introduce additional  
96 uncertainty (and potential bias) into satellite-driven biogenic flux estimates (Ma et al., 2022; Corro et al., 2025;  
97 Glauch et al., 2025). Green coverage within built-up urban areas is similarly high across major Chinese coastal  
98 megacities (e.g., Guangzhou: 43.7 % in 2023; Shenzhen: 44.0 % in 2023; Qingdao: 44.0 % in 2023; Tianjin: 38.2 %  
99 in 2023) (Guangzhou Municipal Bureau of Statistics, 2024; Shenzhen Municipal Bureau of Statistics, 2024;  
100 Qingdao Municipal Bureau of Statistics, 2024; Tianjin Municipal Bureau of Statistics, 2024), implying that  
101 biogenic exchange can be non-negligible when interpreting urban observations. For example, in coastal North  
102 American cities, high-resolution vegetation modeling in New York City indicates that summertime biogenic uptake  
103 can offset up to 40 % of afternoon anthropogenic CO<sub>2</sub> enhancements and can fully balance on-road traffic  
104 contributions (Wei et al., 2022), while a dense-sensor analysis in Los Angeles suggests that daytime biogenic  
105 exchange can consume up to 60 % of fossil-fuel emissions during the peak growing season (Kim et al., 2025).  
106 Recent advances, including emerging atmospheric constraints such as carbonyl sulfide (COS), further demonstrate  
107 the feasibility and value of more robust biogenic quantification in city carbon budgets (Soininen et al., 2025).

108

109 Taken together, three knowledge gaps limit the interpretation of coastal megacity CO<sub>2</sub> observations and their use  
110 for mitigation assessment: (i) how spatiotemporal CO<sub>2</sub> patterns vary across a coastal–urban–suburban gradient; (ii)  
111 how SLB-driven transport and boundary-layer mixing reshape diurnal and seasonal CO<sub>2</sub> signals through seasonally  
112 varying ventilation, boundary-layer depth, and atmospheric stability, which may differ from inland-city regimes;  
113 and (iii) how fossil-fuel and biogenic contributions can be robustly separated, with quantified uncertainty, in a  
114 coastal setting. To bridge these gaps, we investigate Guangzhou (Pearl River Delta, China) as a living laboratory:  
115 high GDP and population indicate strong energy and mobility demand and thus substantial fossil-fuel CO<sub>2</sub>  
116 emissions, while evergreen urban vegetation, a long growing season, and frequent SLB circulation can produce  
117 non-negligible biogenic signals and complex coastal transport. The policy context further elevates the value of  
118 attribution: Guangdong’s emissions-trading system (ETS) has operated since 2013, alongside measures targeting  
119 energy structure, vehicle emissions, building efficiency, and urban greening.

120

121 Given this imperative to track changes in urban emissions and net carbon exchange, we use an observation-driven  
122 framework that complements atmospheric inversion approaches and interprets diurnal–seasonal variability by  
123 combining multi-site in-situ CO<sub>2</sub> and CO measurements with footprint-informed transport analysis (Lin et al., 2003;  
124 Fasoli et al., 2018). Unlike a formal Bayesian 3-D inversion, our framework targets process attribution of observed

125 variability and quantifies robustness through sensitivity tests rather than posterior flux estimates. This approach  
126 emphasizes process-level interpretation of concentration variability while explicitly evaluating key uncertainty  
127 sources. While CO is widely used to infer fossil-fuel CO<sub>2</sub>, it carries inherent uncertainties due to varying emission  
128 ratios (R<sub>CO</sub>), background variability, and atmospheric chemical processing (Turnbull et al., 2011; Chen et al., 2020;  
129 Griffin et al., 2007; Vimont et al., 2019). Footprint estimates are likewise sensitive to meteorological forcing and  
130 boundary-layer representation, and such transport sensitivities may be amplified under complex coastal mesoscale  
131 flows. We therefore quantify uncertainties associated with measurement and background selection, evaluate  
132 robustness to transport-model setup via STILT configuration tests, assess **biogenic biospheric**-consistency using  
133 seasonal vegetation activity (e.g., NDVI), and utilize emission inventories for contextual comparison—using inter-  
134 inventory spread as a plausibility envelope for benchmarking rather than a validation target.

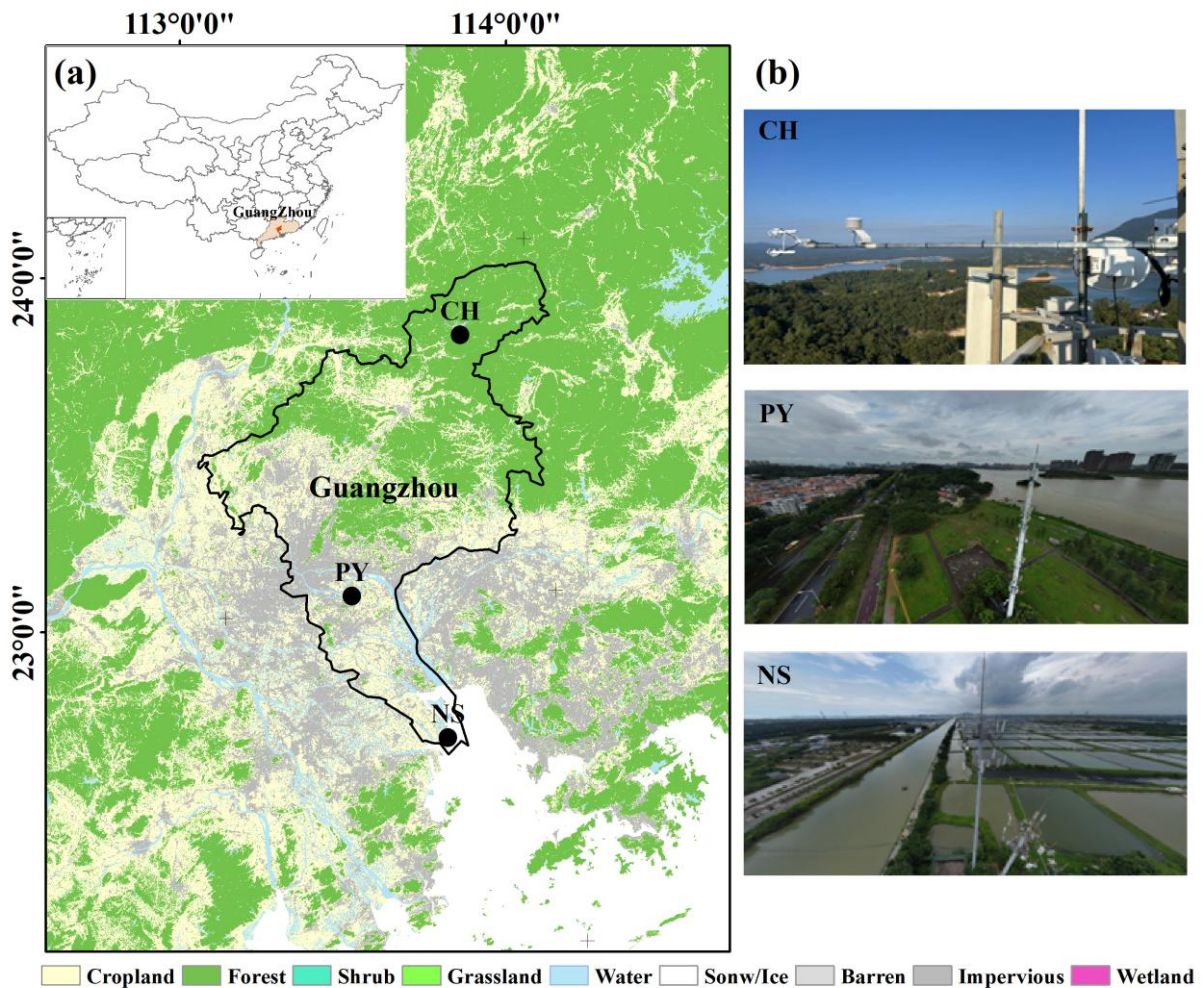
135

136 Accordingly, we aim to: (i) resolve spatiotemporal patterns of CO<sub>2</sub> across three sites spanning near-coastal (NS),  
137 urban-core (PY), and suburban (CH) environments; (ii) quantify how SLB modulates diurnal-seasonal CO<sub>2</sub>  
138 variability and interpret the contrasts in terms of changes in wind ventilation, boundary-layer depth, and seasonally  
139 varying atmospheric stability/stratification; and (iii) partition observed CO<sub>2</sub> enhancements at the urban site (PY)  
140 into fossil-fuel and biogenic components using CO and footprint information, with explicit uncertainty  
141 characterization via measurement/background terms and STILT configuration sensitivity tests.

## 142 **2 Data and methodology**

### 143 **2.1 Observational sites**

144 The high-precision greenhouse gas monitoring network in Guangzhou is illustrated in Fig. 1. Three stations—  
145 Nansha (NS), Panyu (PY), and Conghua (CH) are symmetrically distributed along the city’s predominant south–  
146 north wind axis, representing coastal, urban, and suburban atmospheric conditions, respectively. Site selection  
147 criteria are detailed in the Supplement. All stations employ tower-based sampling at similar heights: NS and PY at  
148 48 m, and CH at 40 m. Monitoring spanned from January 1, 2023, to September 30, 2024. From PY, the straight-  
149 line distances to NS and CH are 54 km and 89 km, respectively.



150

151 **Figure 1.** (a) Geographic locations of the NS, PY, and CH stations, with regional land use classification based on the 30 m  
 152 resolution 2023 land cover product of China (CLCD) (Yang and Huang, 2025). (b) Photographs of each station.

153 The NS station (113.63° E, 22.61° N) is located < 5 km from the coastline. This coastal site is surrounded by  
 154 aquaculture ponds and sparse wetlands. Infrastructure nearby includes the under-construction southern extension  
 155 of Guangzhou Metro Line 18 (NW direction) and the S78 highway (~ 2 km west). The PY station (113.38° E,  
 156 23.03° N) is situated in the densely populated urban core; the tower is adjacent to Guangzhou University Town  
 157 (north) and the Pearl River (south). A city road (~ 100 m north) and the S73 expressway (~ 700 m west) contribute  
 158 to local emissions. The CH station (113.78° E, 23.74° N) is positioned in the northern suburbs. The site is bordered  
 159 by subtropical evergreen broadleaf forests (north), a tourist resort (south), and a tea processing plant. The G45  
 160 highway lies ~ 3 km northwest. According to the Emissions Database for Global Atmospheric Research (EDGAR)  
 161 Community GHG database (EDGAR\_2024\_GHG; 2023; 0.1° × 0.1°) (Crippa et al., 2024), grid-level CO<sub>2</sub> emission  
 162 densities for NS, PY, and CH are 3456, 15244, and 203 ton km<sup>-2</sup> yr<sup>-1</sup>, respectively (Fig. S1 in the Supplement).

## 163 2.2 Monitoring system

164 All three stations are equipped with similar monitoring systems, consisting of sampling modules, calibration

165 modules, gas analyzers, and data acquisition systems. Notably, the NS and PY stations utilize Picarro G2401  
166 greenhouse gas analyzers to measure CO<sub>2</sub>/CH<sub>4</sub>/CO/H<sub>2</sub>O, with a CO<sub>2</sub> measurement precision of < 20 ppb (5 min, 1  
167  $\sigma$ ). The CH station employs an ABB GLA331-GGA greenhouse gas analyzer to measure CO<sub>2</sub>/CH<sub>4</sub>/H<sub>2</sub>O, with a  
168 CO<sub>2</sub> measurement precision of < 25 ppb (5 min, 1  $\sigma$ ). N<sub>2</sub>O and CO are measured using a GLA351-N2OCM analyzer.  
169 Detailed monitoring system and principles of the instruments are provided in the Supplement. Prior to field  
170 deployment, comparative tests were conducted in the laboratory to ensure the analytical performance consistency  
171 of the instruments. Additionally, meteorological sensors (measuring wind speed, direction, humidity, temperature,  
172 and pressure) are installed at the same height as the sampling inlets at NS and PY stations, while the CH station  
173 lacks such sensors. Detailed descriptions of wind field characteristics at NS and PY stations are included in the  
174 Supplement and illustrated in Fig. S2.

### 175 **2.3 Calibration methods**

176 The calibration module comprises two components: working standard curve establishment and target gas  
177 verification. High- and low-concentration standard gases are used to establish calibration curves, while a mid-  
178 concentration standard gas is used for target verification. The target and calibration gases are stored in inert-coated  
179 aluminum cylinders, uniformly supplied by the China National Environmental Monitoring Center. All stations  
180 follow the same calibration protocol: (1) weekly calibration curve establishment: high- and low-concentration gases  
181 are injected for 30 minutes each, with the final 5 minutes of instrument response used for calibration; (2) target gas  
182 verification every 12 h: mid-concentration gas is injected for 30 minutes, with the final 5 minutes of response used  
183 for verification; (3) re-calibration is triggered if the residual value (H) from target verification exceeds  $\pm 0.2$  ppm.  
184

185 Calibration curves are derived from the instrument's response to calibration gas, yielding a linear calibration  
186 equation:

$$187 \quad Y = A \times X - B, \quad (1)$$

188 where A, B are calibration coefficients. Calibrated CO<sub>2</sub> (CO<sub>2,k</sub>) is calculated by:

$$189 \quad CO_{2,k} = A \times CO_{2,m} - B, \quad (2)$$

190 where CO<sub>2,m</sub> is the measured response. Daily 12 h target gas verification is conducted to assess analyzer accuracy  
191 and stability by calculating the residual H:

$$192 \quad H = (A \times CO_{2,c} - B) - CO_{2,n} . \quad (3)$$

193 where CO<sub>2,n</sub> is the standard CO<sub>2</sub> concentration of the target gas, and CO<sub>2,c</sub> is the analyzer response/reading to the  
194 target gas.

195

196 To ensure high-precision and stable monitoring results, periods with  $|H| \leq 0.1$  ppm are prioritized. Measurement  
197 uncertainties for the analyzers at NS, PY, and CH stations, calculated as the standard deviation (SD) of H (Yang et  
198 al., 2021), are 0.04, 0.02, and 0.04 ppm, respectively. In addition to daily calibration, maintenance personnel  
199 conduct weekly inspections of instruments and station facilities, including checks on power supply stability, data  
200 logger functionality, and industrial control computer status. Consumables (e.g., filters) are replaced as needed, and  
201 emergency repairs or instrument overhauls are performed when necessary. Any instrument downtime caused by  
202 internal or external factors is documented in maintenance logs, and affected data is flagged. Throughout the  
203 monitoring period, all three stations maintained data validity rates exceeding 90 %.

#### 204 **2.4 Sea–land breeze identification**

205 The straight-line distances from the NS, PY, and CH stations to the coastline are 4, 58, and 130 km, respectively.  
206 The NS station, closest to the coast, was selected to study Guangzhou’s sea–land breeze (SLB) circulation. Prior to  
207 SLB identification, local and background winds must be differentiated, as tower-measured winds (Fig. S2 in the  
208 Supplement) represent superimposed local and background wind fields, where strong background winds can  
209 obscure SLB signals (Qiu and Fan, 2013). The following equations distinguish background winds from local winds  
210 (Sun et al., 2022; Shen et al., 2019):

$$211 \quad U_b = \overline{\sum_{i=0}^{23} U_i}, \quad (4)$$

$$212 \quad V_b = \overline{\sum_{i=0}^{23} V_i}, \quad (5)$$

$$213 \quad U_l = U_o - U_b, \quad (6)$$

$$214 \quad V_l = V_o - V_b. \quad (7)$$

215 where  $U_o$  and  $V_o$  are the observed wind fields from the tower,  $U_b$  and  $V_b$  denote background winds, and  $U_l$  and  $V_l$   
216 represent local winds.

217

218 A sea–land breeze day (SLBD) is defined as any 24 h period exhibiting a distinct transition from sea breezes during  
219 the day to land breezes at night (Xiao et al., 2023). SLB identification criteria vary regionally due to differences in  
220 topography and coastline geometry (Huang et al., 2025). Guided by the SLB criteria in Supplementary Table S1  
221 and historical patterns for the Pearl River Estuary (Qiu and Fan, 2013; Zhang et al., 2024; Mai et al., 2024b), we  
222 define for the north-shore site (NS) directional sectors of  $112\text{--}202^\circ$  for the sea breeze and  $302\text{--}45^\circ$  for the land  
223 breeze. The corresponding detection windows are 12:00–20:00 LT (sea breeze) and 01:00–09:00 LT (land breeze),

224 consistent with regional SLB climatologies. Directional persistence is evaluated using the local-wind direction. The  
225 wind-speed screen is applied to the observed wind-speed magnitude at 48 m. A day is labeled as an SLB day only  
226 if all the following conditions are satisfied: (1) Directional persistence: within each window, the local wind  
227 direction (from the decomposed local component) stays inside the corresponding sector for  $\geq 4$  h, or for  $\geq 4$  h within  
228 any running 5 h window; and (2) Weak-forcing screen: for the same candidate SLB day, the observed wind-speed  
229 magnitude at 48 m must remain  $< 10 \text{ m s}^{-1}$  at every hour of that day (i.e., no hourly value exceeds  $10 \text{ m s}^{-1}$ ). This  
230 conservative cap follows coastal-China SLB climatologies and is intended to exclude strongly forced days (Qiu  
231 and Fan, 2013; Sun et al., 2022; Huang et al., 2025; Zhang et al., 2024). Otherwise, the day is designated a non-  
232 SLB day (NSLBD).

233

234 Together, these two requirements reduce the likelihood of misclassification under strongly forced conditions. Days  
235 dominated by synoptic forcing or tropical-cyclone peripheries often show a prolonged anomalous wind regime  
236 rather than a clear diurnal reversal (Atkins and Wakimoto, 1997; Allouche et al., 2023). To explicitly assess residual  
237 tropical-cyclone (TC) contamination, we cross-referenced the SLB calendar with 2023 Pearl River Delta  
238 (PRD)/Guangzhou TC impact windows compiled from the official Guangdong–Hong Kong–Macao Greater Bay  
239 Area (GBA) Climate Monitoring Bulletin (Table S2). For each TC, impact start/end are defined as the first/last  
240 local dates on which the bulletin reports PRD/Guangzhou impacts or advisories attributable to that system  
241 (including peripheral rainbands/gusts). Because the bulletin is date-based, we conservatively treat the entire day  
242 within each window as potentially TC-influenced. Only one SLBD (2 Sep 2023) falls within these windows;  
243 excluding it leaves results unchanged.

## 244 **2.5 Estimation of $\text{CO}_2^{\text{tot}}$ , $\text{CO}_2^{\text{ff}}$ , and $\text{CO}_2^{\text{bio}}$**

245 The observed  $\text{CO}_2$  concentration enhancements at tall-tower receptor sites represent the integrated influence of  
246 upwind surface fluxes transported by atmospheric advection and mixing (Lin et al., 2003). Consequently, upwind  
247 carbon emissions can be inferred from site-specific enhancement measurements coupled with their corresponding  
248 atmospheric footprints. Here we apply an observation-driven framework that combines concentration-enhancement  
249 observations with transport-model footprints to estimate total  $\text{CO}_2$  ( $\text{CO}_2^{\text{tot}}$ ) and CO ( $\text{CO}^{\text{tot}}$ ) surface fluxes, and to  
250 further derive fossil-fuel ( $\text{CO}_2^{\text{ff}}$ ) and biogenic ( $\text{CO}_2^{\text{bio}}$ ) components using the site-specific  $\Delta\text{CO}/\Delta\text{CO}_2$  relationship  
251 ( $R_{\text{CO}}$ ), without relying on any a priori emissions inventory. The required inputs are limited to enhancement  
252 observations at the receptor sites and atmospheric footprints, consistent with previous regional flux quantifications  
253 for  $\text{CO}_2$ ,  $\text{CH}_4$ , and CO (Mitchell et al., 2018; Lin et al., 2021; Wu et al., 2022a). Emission inventories are used only

254 for site-context characterization (Sect. 2.1) and, subsequently, for an independent bottom-up plausibility envelope  
 255 for winter-afternoon flux estimates (Sect. 3.5), rather than as priors or validation targets.  $CO_{2tot}$  and  $CO_{tot}$  are  
 256 calculated as:

$$257 \quad CO_{2tot} = \frac{CO_{2,s}obs - CO_{2}bg}{\sum_i Footprint_{i,s}}, \quad (8)$$

$$258 \quad CO_{tot} = \frac{CO_{s}obs - CO_{bg}}{\sum_i Footprint_{i,s}}, \quad (9)$$

259 The numerators are hourly  $CO_2$  and CO concentration enhancements ( $\Delta CO_2$  and  $\Delta CO$ ) at station  $s$ , where  $CO_{2,s}obs$   
 260 and  $CO_{s}obs$  represent observed  $CO_2$  and CO concentrations, while  $CO_{2}bg$  and  $CO_{bg}$  denote urban background  
 261 concentrations (detailed in the Supplement). The denominators are hourly total atmospheric footprints  
 262 ( $\sum_i Footprint_{i,s}$ ), where  $i$  denotes backward particle release time from the receptor. Due to challenges in modeling  
 263 mixed-layer depths during nighttime, morning, and evening, flux analysis focuses on afternoon hours (12:00–16:00)  
 264 (Boon et al., 2016; Mitchell et al., 2018; Lin et al., 2021). Daily-scale  $CO_{2tot}$  and  $CO_{tot}$  are derived by dividing  
 265 the mean afternoon  $\Delta CO_2$  and  $\Delta CO$  by the corresponding mean  $\sum_i Footprint_{i,s}$ . The footprint quantifies the  
 266 sensitivity of concentration enhancements at the observation site to upwind surface fluxes, as detailed in Sect. 2.5.1.  
 267  $\Delta CO_2$  is in units of [ppm], while footprint is in [ppm / ( $\mu mol m^{-2} s^{-1}$ )], so  $CO_{2tot}$ , the quotient between the two  
 268 quantities, is in flux units of [ $\mu mol m^{-2} s^{-1}$ ].

269

270 Anthropogenic  $CO_2$  emissions ( $CO_{2ff}$ ) are derived from  $CO_{tot}$  and the CO/ $CO_2$  emission ratio ( $R_{CO}$ ), where  $R_{CO}$  is  
 271 determined from real-time tower-measured data, as described in detail in Sect. 3.4:

$$272 \quad CO_{2ff} = \frac{CO_{tot}}{R_{CO}}, \quad (10)$$

273 Biogenic fluxes ( $CO_{2bio}$ ) are calculated as residuals:

$$274 \quad CO_{2bio} = CO_{2tot} - CO_{2ff}. \quad (11)$$

275 Positive  $CO_{2bio}$  values indicate biogenic carbon emissions, while negative values denote carbon uptake, reflecting  
 276 the dual role of urban biospheres as  $CO_2$  sources and sinks (Kim et al., 2025).

### 277 **2.5.1 Atmospheric transport model**

278 To trace air mass sources entering the urban domain and reaching observation sites, and to assess  $CO_2$  emissions  
 279 corresponding to observed concentration enhancements, the Stochastic Time-Inverted Lagrangian Transport model  
 280 (STILT-Rv2) was employed for atmospheric transport simulations, driven by meteorological fields from the  
 281 Weather Research and Forecasting Model (WRFv4.1.1). In this study, STILT serves two purposes: (1) providing

282 airmass trajectories for identifying marine background concentrations in Guangzhou, and (2) generating  
283 atmospheric footprints for quantifying total CO<sub>2</sub> and CO emissions.

284

285 The STILT model simulates atmospheric transport by releasing a set of air particles backward in time from the  
286 receptor location at the observation height. These particles are tracked spatially and temporally as they disperse  
287 upwind. The resulting trajectories delineate source regions influencing the receptor site and quantify the sensitivity  
288 of observed concentrations to upwind surface fluxes, termed "source–receptor relationships" or "atmospheric  
289 footprints" (Lin et al., 2003; Fasoli et al., 2018). Footprints represent the contribution of upwind sources/sinks to  
290 downwind concentration changes, with higher sensitivities near receptors or under stable wind conditions, where  
291 boundary layer airmasses interact more directly with surface fluxes (Wu et al., 2022a). For this study, 500 particles  
292 were released at 48 m (PY station) heights, and traced backwards in time for 72 h. Footprints were computed at  
293 0.08° × 0.08° spatial resolution. Periods with total footprint sensitivities ( $\sum_i \text{Footprint}_i$ ) below the 10th percentile  
294 were excluded, indicating low sensitivity to regional surface fluxes (Lin et al., 2021).

295

296 To evaluate whether STILT setup choices could bias the inferred fluxes, we performed targeted wintertime  
297 sensitivity experiments at PY using paired daily comparisons (n = 18). Starting from the baseline (500 particles,  
298 0.08° grid, 72 h backward), we independently varied (1) particle number (1000, 2000), (2) grid resolution (0.05°,  
299 0.10°), and (3) backward duration (96 h, 120 h). For each variant we recomputed footprints, reran the flux-  
300 estimation framework, and compared paired daily afternoon means (12:00–16:00 LT) of CO<sub>2</sub>tot, CO<sub>2</sub>ff and CO<sub>2</sub>bio  
301 to the baseline using percent differences, Pearson r, and paired t-tests. Percent differences quantify effect size,  
302 Pearson r assesses day-to-day consistency, and paired t-tests evaluate detectability of systematic mean shifts. This  
303 paired-day design isolates transport-model parameter effects from day-to-day meteorology and observation  
304 sampling.

### 305 **2.5.2 Uncertainty sources**

306 Uncertainties associated with the emission estimates inferred from Eqs. (12)–(14) primarily arise from four sources:  
307 (1) observational uncertainty, (2) background concentration uncertainty, (3) atmospheric transport (footprint)  
308 uncertainty, and (4) R<sub>CO</sub>-related uncertainty. We do not explicitly propagate transport/footprint uncertainty within  
309 the analytical error propagation of Eqs. (12)–(14); instead, we evaluate sensitivity to transport-model setup using a  
310 winter paired-day STILT sensitivity analysis (Sect. 2.5.1; Sect. 3.5; Fig. 11). Residual transport biases (e.g., winds  
311 and boundary-layer mixing) remain unquantified and may bias the inferred fluxes, thereby contributing to

312 inventory–observation differences when benchmarking against independent bottom-up inventories, alongside  
 313 emission-inventory uncertainty and the representativeness mismatch between footprint-weighted enhancements  
 314 and unweighted inventory means (discussed further in Sect. 3.5). Uncertainty associated with  $R_{CO}$  is not explicitly  
 315 propagated as a formal regression-parameter uncertainty in this study; because  $R_{CO}$  is derived from CO and CO<sub>2</sub>  
 316 enhancements, its uncertainty is expected to be driven mainly by uncertainties in the underlying enhancements  
 317 (items 1–2) and scatter in the site-specific relationship. Among the quantified terms, uncertainties in CO<sub>2</sub>tot are  
 318 dominated by observational and background concentration errors. Uncertainties in CO<sub>2</sub>ff are additionally affected  
 319 by  $R_{CO}$ -related variability, while uncertainties in CO<sub>2</sub>bio and the CO<sub>2</sub>bio/CO<sub>2</sub>ff offset ratio are propagated from  
 320 CO<sub>2</sub>tot and CO<sub>2</sub>ff. Accordingly, the combined uncertainty term is calculated as:

$$321 \quad E_u^2 = OBS_{u,c}^2 + BG_u^2, \quad (12)$$

322 where  $OBS_{u,c}$  represents uncertainty in urban atmospheric observations, and  $BG_u$  represents uncertainty in urban  
 323 background concentrations. We cannot accurately quantify all error sources involved in instrumental measurements;  
 324 some minor error sources (e.g., uncertainty related to water vapor) may be negligible, while the primary uncertainty  
 325 originates from discrepancies between measured concentrations and calibration standards (Verhulst et al., 2017).  
 326 Here,  $OBS_{u,c}$  is calculated as the standard deviation (SD) of residuals H (Yang et al., 2021). For urban background  
 327 uncertainties:

$$328 \quad BG_{u,co2}^2 = CT_{co2,r}^2 + CT_{co2,s}^2, \quad (13)$$

$$329 \quad BG_{u,co}^2 = OBS_{co,r}^2 + OBS_{co,s}^2. \quad (14)$$

330 CO<sub>2</sub> background uncertainty ( $BG_{u,co2}$ ) combines the absolute monthly smoothed residuals ( $CT_{co2,r}$ ) and variability  
 331 (SD) of monthly CO<sub>2</sub> concentrations ( $CT_{co2,s}$ ) from CarbonTracker (CT). Similarly, CO background  
 332 uncertainty ( $BG_{u,co}$ ) is derived from monthly smoothed residuals ( $OBS_{co,r}$ ) and variability ( $OBS_{co,s}$ ) of in situ  
 333 observations.

334

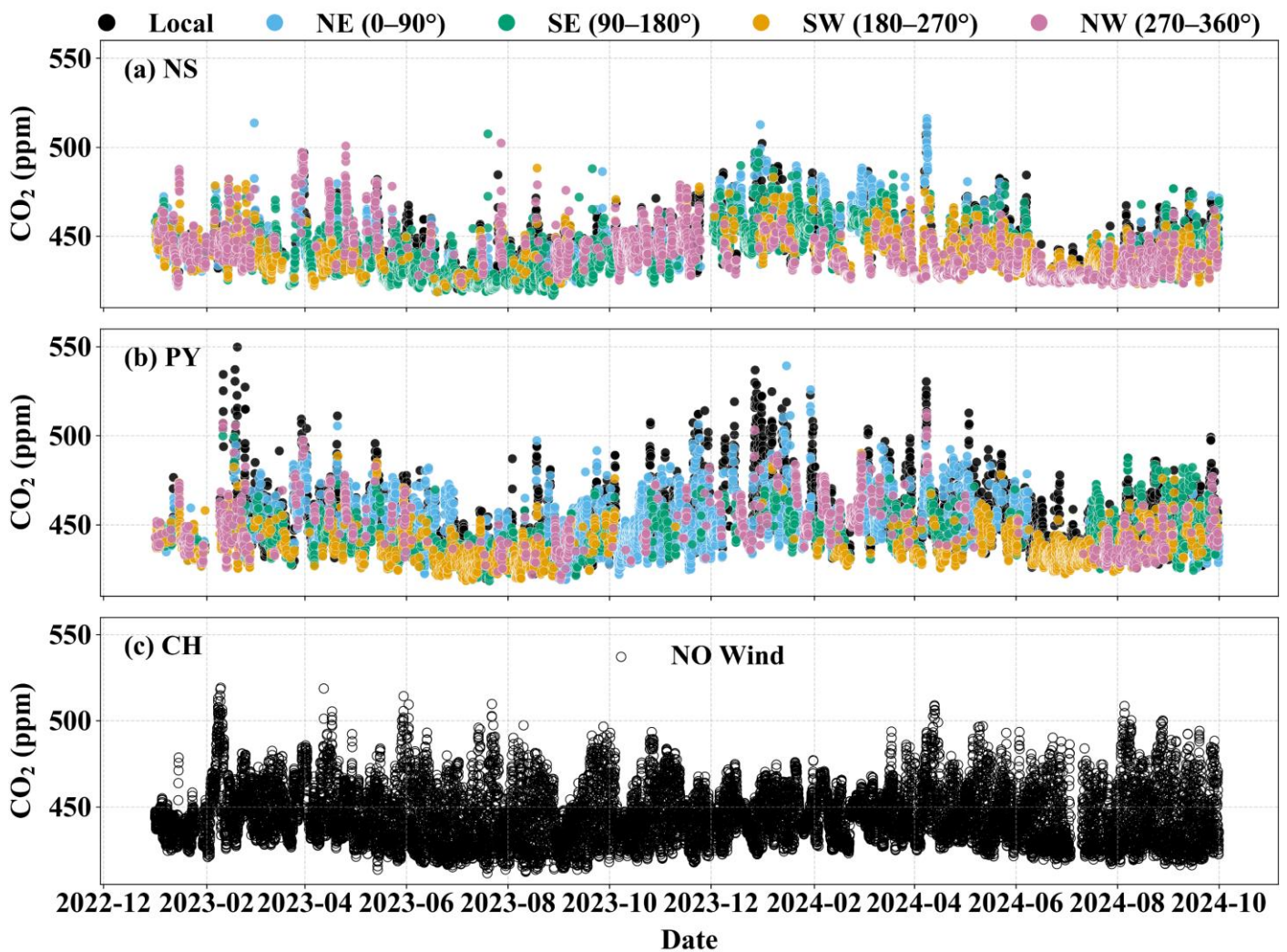
335 To guard against bias from transport settings, the paired-day sensitivity analysis is conducted relative to the baseline;  
 336 we treat effect sizes and 95 % confidence intervals (CIs) as primary quantities and report p-values only to indicate  
 337 detectability given  $n = 18$ , with quantitative outcomes presented in Sect. 3.5 and Fig. 11.

### 338 **3 Results and discussion**

#### 339 **3.1 Spatiotemporal patterns of atmospheric CO<sub>2</sub>**

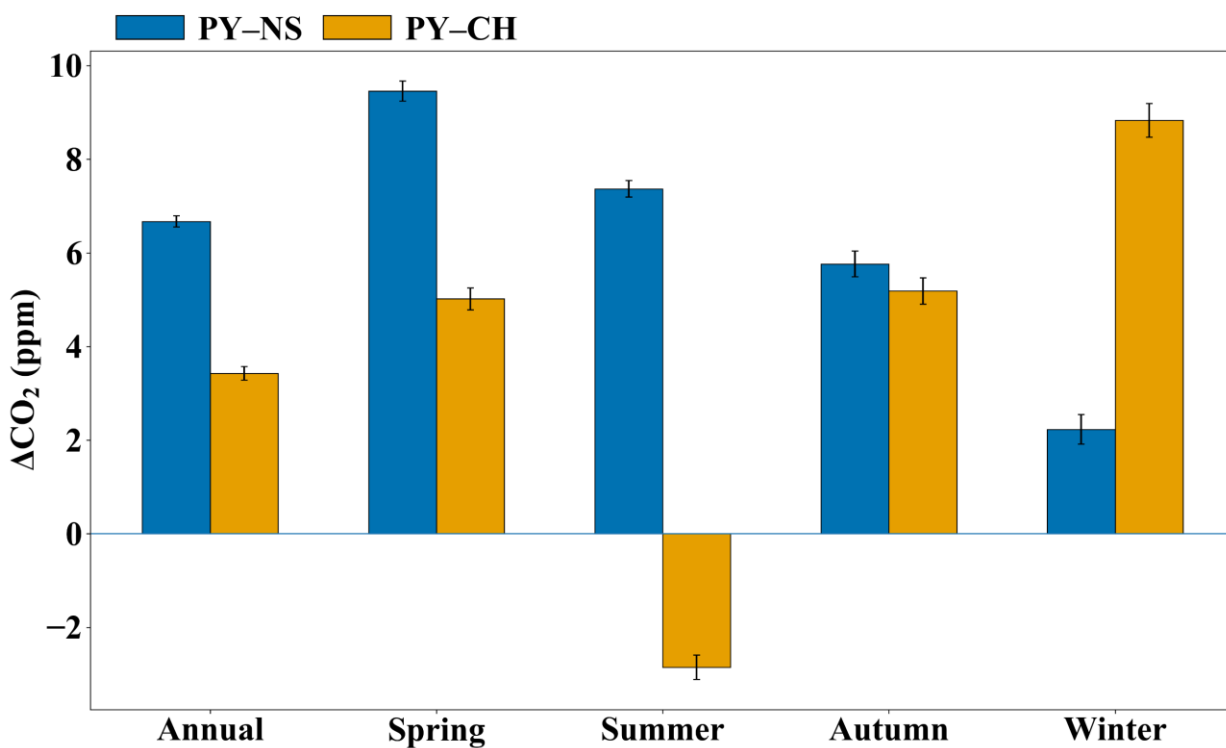
340 Figure 2 presents the hourly mean time series of atmospheric CO<sub>2</sub> concentrations at the NS, PY, and CH stations

341 in Guangzhou from January 1, 2023, to September 30, 2024. To assess wind field impacts on CO<sub>2</sub> variability (Fig.  
 342 S2), concentrations were classified into five categories: local (wind speed < 1.5 m s<sup>-1</sup>) and four directional sectors  
 343 (wind speed ≥ 1.5 m s<sup>-1</sup>) defined as NE (0–90°), SE (90–180°), SW (180–270°), and NW (270–360°). All stations  
 344 exhibited significant temporal variability, with standard deviations (SD) of 13.90 (NS), 15.92 (PY), and 16.05 ppm  
 345 (CH), consistent with urban and suburban observations in Hangzhou, Beijing, Xi'an, and Seoul (Park et al., 2021;  
 346 Yang et al., 2021; Chen et al., 2024; Liu et al., 2025). PY showed the highest CO<sub>2</sub> levels and variability, driven  
 347 predominantly by local-type emissions under low wind speeds. In contrast, the NS coastal station exhibited  
 348 elevated concentrations during northerly winds (NW/NE). Seasonal wind effects were pronounced:  
 349 summer southerly winds (SW/SE) generally reduced CO<sub>2</sub> at PY and NS (most notably at NS near the coast), while  
 350 winter northerly winds (NW/NE) often increased CO<sub>2</sub> at NS.



351  
 352 **Figure 2.** Time series of atmospheric CO<sub>2</sub> concentrations at the (a) NS, (b) PY, and (c) CH stations, points are color-  
 353 coded by wind category: local conditions (wind speed < 1.5 m s<sup>-1</sup>) and four directional sectors for winds ≥ 1.5 m s<sup>-1</sup> (NE, 0–  
 354 90°; SE, 90–180°; SW, 180–270°; NW, 270–360°). For CH, wind-direction classification is not shown and the time series is  
 355 plotted without sector coloring.

356 Urban–rural CO<sub>2</sub> gradients vary globally due to differences in economic activity, population density, land use, and  
 357 energy infrastructure, reflecting heterogeneous urban carbon emissions (Gao et al., 2022). To further illustrate this  
 358 spatial contrast and its seasonality, we summarized the urban–suburban/coastal gradients across the full record and  
 359 report annual and seasonal means in Fig. 3. In Guangzhou, mean CO<sub>2</sub> concentration differences between PY and  
 360 NS/CH were 6.67 and 3.43 ppm, respectively, forming a distinct "urban dome" (urban > suburban > coastal). The  
 361 NS–CH difference (3.44 ppm) highlights comparable gradients between suburban and coastal zones. This gradient  
 362 mirrors Los Angeles’s coastal megacity profile but with a smaller magnitude (Verhulst et al., 2017). Guangzhou’s  
 363 urban–suburban difference (3.43 ppm) aligns with Hangzhou’s 2021 observations (4.96 ppm) (Chen et al., 2024)  
 364 but is lower than Nanjing (8.1 ppm, 2014) and Beijing (12.4 ppm, 2018–2019) (Gao et al., 2018; Yang et al., 2021).  
 365 It remains far smaller than Shanghai (55.1 ppm, 2014) and Baltimore (66.0 ppm, 2002–2006) (Pan et al., 2016;  
 366 George et al., 2007). Over time, urban emissions may stabilize as suburban populations and fossil fuel demand  
 367 grow, potentially narrowing urban–suburban CO<sub>2</sub> differences (Mitchell et al., 2018). For instance, Hangzhou’s  
 368 reduced gradient reflects urbanization-driven energy consumption, where suburban monitoring captures urban  
 369 emission influences (Chen et al., 2024).



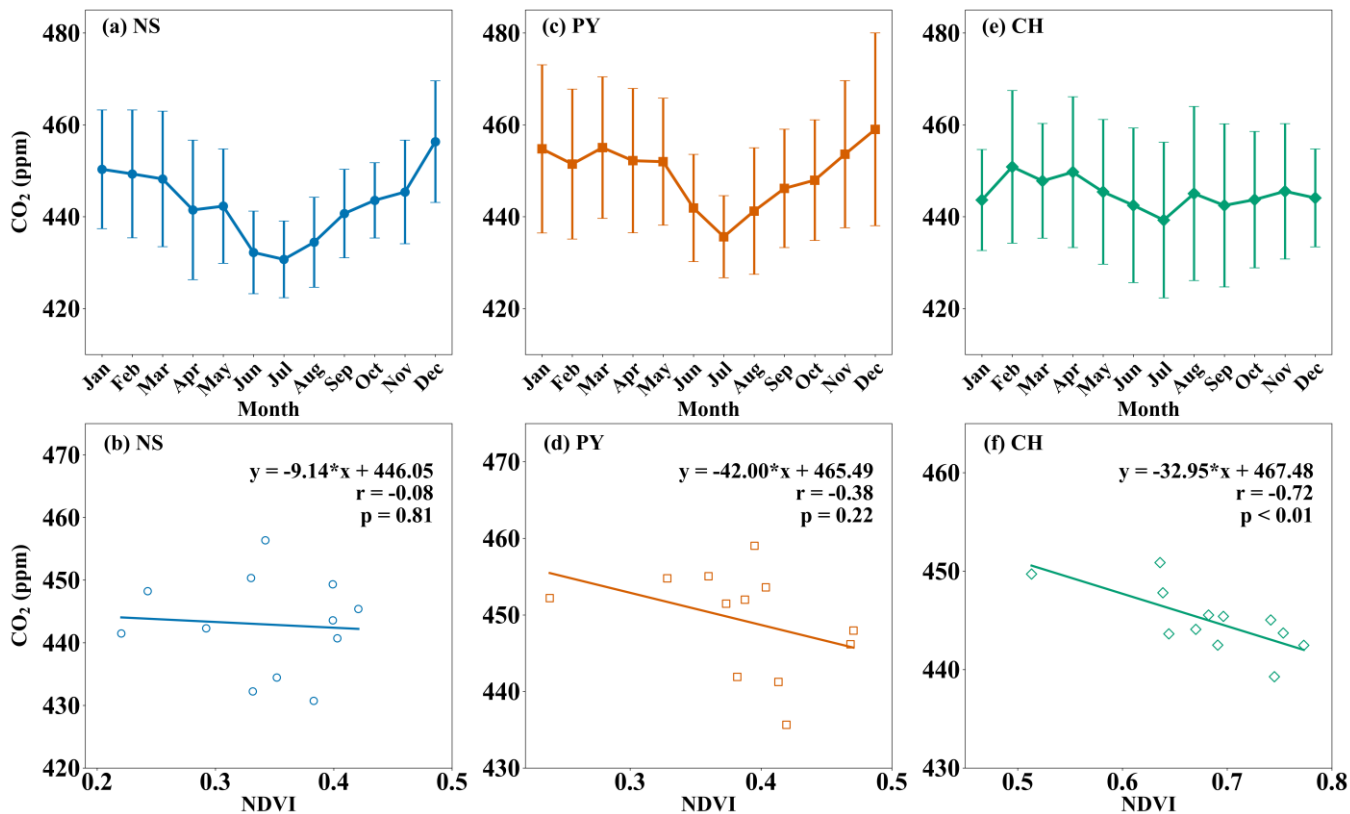
370  
 371 **Figure 3.** Urban–suburban/coastal CO<sub>2</sub> gradients in Guangzhou. Annual and seasonal mean concentration differences  
 372 ( $\Delta\text{CO}_2$ , ppm) between the urban site (PY) and the coastal site (NS) (PY–NS) and between PY and the suburban site (CH)  
 373 (PY–CH). Seasons are defined as **spring** (Mar–May), **summer** (Jun–Aug), **autumn** (Sep–Nov), and **winter** (Dec–Feb). Error  
 374 bars denote  $\pm 1$  standard error (SE).

375 Figure 3 further shows that these spatial gradients are strongly season-dependent. PY–NS remains positive year-

376 round but is smallest in winter (2.23 ppm), when prevailing northerlies elevate CO<sub>2</sub> at the coastal NS site and reduce  
377 the urban–coastal contrast, consistent with Fig. 2. PY–CH is more strongly seasonally modulated: it peaks in winter  
378 (8.83 ppm) but reverses sign in summer (–2.86 ppm), when southerly (marine-influenced) flow more frequently  
379 ventilates PY (SW/SE sectors in Fig. 2) and the CH summertime enhancement may reflect a northward-displaced  
380 urban influence plus biogenic/boundary-layer modulation (Sect. 3.1.1; Sect. 3.3). Spring and autumn show  
381 intermediate positive PY–CH (~ 5 ppm), while PY–NS peaks in spring (9.46 ppm), consistent with enhanced  
382 coastal ventilation under southerly influence. Together, these gradients indicate a seasonally displaced CO<sub>2</sub> “dome”  
383 in this coastal setting, where the highest CO<sub>2</sub> within our network can occur outside the urban core, complementing  
384 the site-level seasonal cycles discussed in Sect. 3.1.1. This coastal, seasonally displaced CO<sub>2</sub> dome contrasts with  
385 patterns more commonly reported in inland megacity networks, where enhancements are typically strongest at the  
386 most urbanized sites relative to suburban/background stations (Xueref-Remy et al., 2018; Yang et al., 2021; Chen  
387 et al., 2024).

### 388 **3.1.1 Seasonal variability of atmospheric CO<sub>2</sub>**

389 Figure 4 illustrates the monthly mean variations in atmospheric CO<sub>2</sub> concentrations at the NS, PY, and CH stations  
390 in Guangzhou, alongside their correlations with the Normalized Difference Vegetation Index (NDVI). NDVI data  
391 at 1 km × 1 km spatial resolution were obtained from NASA’s EOSDIS Land Processes Distributed Active Archive  
392 Center (Didan, 2015), with values within a 3 km radius buffer around each station center used for comparative  
393 analysis. All three stations exhibited consistent seasonal CO<sub>2</sub> patterns, with higher concentrations in winter/spring  
394 and lower values in summer/autumn, mirroring observations in Hangzhou (Chen et al., 2024). These variations  
395 arise from the combined effects of (1) seasonal biogenic flux cycles, (2) anthropogenic emission variability, and (3)  
396 boundary layer height dynamics (Xueref-Remy et al., 2018). Enhanced vegetation photosynthesis during warmer  
397 months (summer/autumn, Table S3 in the Supplement) strengthens biogenic carbon sinks, while higher boundary  
398 layer depths (Fig. S6 in the Supplement) and southerly marine air masses (Fig. 2) promote atmospheric mixing and  
399 CO<sub>2</sub> dispersion.



400

401 **Figure 4.** Monthly mean CO<sub>2</sub> concentrations (upper panels) and their correlations with the Normalized Difference  
 402 Vegetation Index (NDVI) (lower panels) for the (a–b) NS, (c–d) PY, and (e–f) CH stations. Error bars indicate ± 1 standard  
 403 deviation (SD).

404 The amplitudes of the seasonal variation of CO<sub>2</sub> at NS, PY, and CH are 25.63, 23.38, and 11.59 ppm, respectively.  
 405 NS and PY peaked in December and troughed in July, whereas CH peaked in February and troughed in July. NS's  
 406 large amplitude reflects its extreme December highs and July lows. In December, prevailing northerly winds (Figs.  
 407 2a and S2a) transported urban emissions to downwind NS, narrowing its CO<sub>2</sub> difference with PY to 2.68 ppm.  
 408 Conversely, July saw NS's CO<sub>2</sub> concentrations fall to the lowest among all stations—4.93 ppm and 8.56 ppm below  
 409 PY and CH, respectively—establishing a south-to-north increasing gradient (coastal < urban < suburban). This  
 410 gradient aligns with marine-influenced southerly air masses, which dilute coastal CO<sub>2</sub> while transporting urban  
 411 emissions northward, potentially accumulating CO<sub>2</sub> in northern suburbs. This south–north pattern is consistent with  
 412 the seasonal mean gradients in Fig. 3, which summarize how the urban–coastal contrast weakens in winter and how  
 413 the urban–suburban gradient can be seasonally displaced in summer.

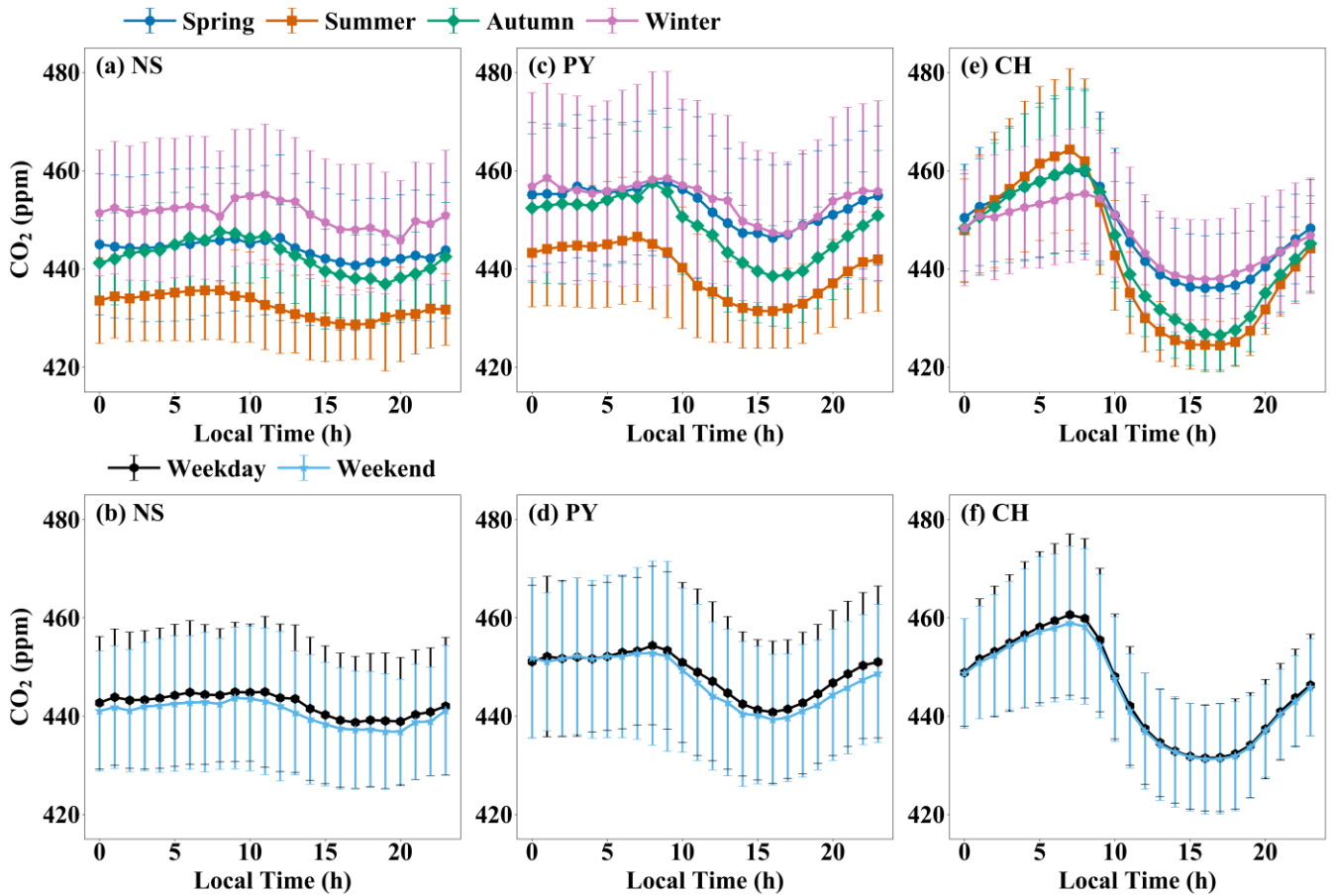
414

415 Although CH exhibits strong biogenic coupling (NDVI–CO<sub>2</sub> correlation: –0.72; Fig. 4f), NS shows an opposite  
 416 seasonal contrast relative to CH (–9.80 ppm in summer; +5.80 ppm in winter), pointing to transport- and boundary-  
 417 layer-driven variability at the coastal site. At NS, the NDVI–CO<sub>2</sub> correlation is weak (–0.08) and NDVI varies  
 418 within a narrow range (0.22–0.42), indicating limited local biogenic control, whereas seasonal shifts in marine–

419 continental transport (summer dilution vs. winter urban outflow) and boundary-layer depth jointly modulate  
420 dilution and accumulation (Figs. 2 and S6). In February, CH recorded its annual CO<sub>2</sub> maximum, driven by  
421 vegetation respiration during early growth stages and elevated emissions from fireworks around the Lunar New  
422 Year, as CH's location falls outside Guangzhou's fireworks restriction zones  
423 ([https://www.gz.gov.cn/gfxwj/qjgfxwj/chq/qf/content/post\\_7198980.html](https://www.gz.gov.cn/gfxwj/qjgfxwj/chq/qf/content/post_7198980.html), last access: 18 June 2025). This  
424 interpretation is supported by CO, a tracer for combustion-derived CO<sub>2</sub> (Newman et al., 2013; Che et al., 2022a):  
425 CH's CO concentrations also peaked in February due to firework emissions, whereas other sites peaked in  
426 December (Fig. S7 in the Supplement).

### 427 **3.1.2 Diurnal variations of atmospheric CO<sub>2</sub>**

428 The diurnal patterns of atmospheric CO<sub>2</sub> concentrations at NS, PY, and CH stations in Guangzhou consistently  
429 exhibited lower daytime and higher nighttime values (Fig. 5). This is attributed to the shallow nocturnal boundary  
430 layer, which traps anthropogenic and biogenic fluxes near the surface, elevating CO<sub>2</sub> levels. After sunrise, surface  
431 heating deepens the boundary layer, diluting surface emissions and entraining free tropospheric air with lower CO<sub>2</sub>  
432 concentrations. Concurrently, daytime photosynthetic uptake further reduces near-surface CO<sub>2</sub> (Mitchell et al.,  
433 2018). We further evaluate urban–suburban–coastal differences in these processes. At PY, the CO<sub>2</sub> peak occurred  
434 at 08:00–09:00, aligning with morning traffic peaks, reflecting dominant anthropogenic influences. CH's peak  
435 appeared 1–2 h earlier than PY due to its longitudinal and elevational position, where earlier sunrise accelerates the  
436 breakup of the nocturnal stable boundary layer. Both PY and CH reached minima at 16:00–17:00, likely linked to  
437 afternoon photosynthetic activity. NS exhibited irregular peak/valley timing.



438  
 439 **Figure 5.** Diurnal CO<sub>2</sub> variations at the (a–b) NS, (c–d) PY, and (e–f) CH stations, shown across seasons (upper panels)  
 440 and weekdays/weekends (lower panels). Seasons are defined as spring (Mar–May), summer (Jun–Aug), autumn (Sep–Nov),  
 441 and winter (Dec–Feb). Error bars indicate ± 1 SD. The corresponding CO diurnal cycles are shown in Fig. S9.

442 Diurnal amplitudes at CH and PY were larger in summer/autumn than winter/spring, driven by vegetation activity  
 443 and boundary layer dynamics (Fig. S8 in the Supplement). Summer/autumn conditions in Guangzhou—abundant  
 444 light, warmth, and rainfall—optimize vegetation growth, enhancing daytime photosynthesis and nighttime  
 445 respiration (Dusenge et al., 2019). Optimal canopy temperatures for subtropical evergreen forests (~ 30 °C) (Liu  
 446 et al., 2015) align with CH/PY’s summer/autumn daytime temperatures (Table S3), explaining their amplified  
 447 amplitudes. However, the diurnal amplitude of CO<sub>2</sub> at CH in summer and autumn is 2.63 times and 1.77 times that  
 448 at PY, respectively. The diurnal amplitude of atmospheric CO<sub>2</sub> concentration at CH in summer is 39.90 ppm, which  
 449 is close to the diurnal amplitude of CO<sub>2</sub> concentration in the suburbs of Hangzhou in summer (35.29 ppm) (Chen  
 450 et al., 2024). Despite similar temperatures, CH’s larger NDVI range and stronger NDVI–CO<sub>2</sub> correlation (–0.72 vs.  
 451 PY; Figs. 4d and f) highlight greater biogenic dominance, with pronounced daytime uptake and nighttime  
 452 respiration. NS showed the smallest diurnal amplitudes across seasons (e.g., 5.60 ppm in summer), attributable to  
 453 sparse vegetation (low NDVI: 0.22–0.42) and frequent summer southerly marine air masses, which dilute coastal  
 454 CO<sub>2</sub>.

455

456 Figure 5B contrasts weekday–weekend diurnal CO<sub>2</sub> patterns. All stations generally showed higher weekday  
457 concentrations, diverging from Hangzhou and Beijing (Yang et al., 2021; Chen et al., 2024) but aligning with Paris  
458 and Boston (Briber et al., 2013; Xueref-Remy et al., 2018). At CH, the daytime weekday–weekend contrast is small.  
459 This could reflect a weak anthropogenic weekday–weekend signal relative to other sources of variability, but it  
460 does not uniquely diagnose source dominance because transport and boundary-layer mixing may dilute or mask  
461 weekday–weekend differences. At PY, the clearer daytime weekend decrease is consistent with reduced on-road  
462 activity in the urban core. At NS, weekday CO<sub>2</sub> remains higher across much of the day, which may reflect weekday-  
463 intensified construction and port-related logistics in the surrounding area (for example, the Metro Line 18 extension  
464 and operations near the Nansha Container Terminal Phase III, ~ 5 km east), superimposed on transport and mixing  
465 effects.

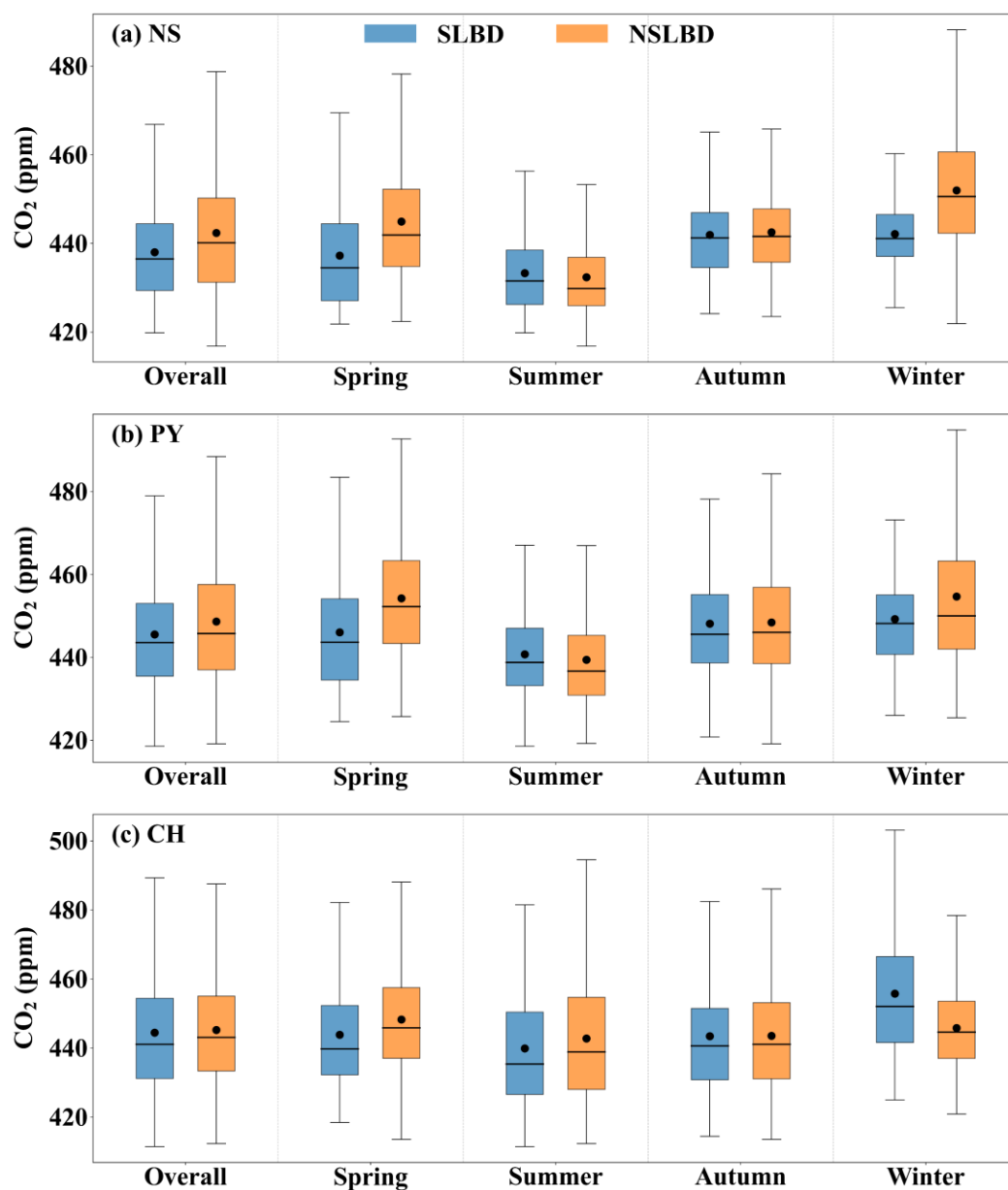
466

467 To corroborate the combustion contribution to the CO<sub>2</sub> diurnal cycle, we examined synchronous CO measurements  
468 (Fig. S9 in the Supplement). At all sites, CO shows a consistent seasonal ordering (winter highest, summer lowest),  
469 and its morning maximum at PY (typically 08:00–10:00) coincides with the CO<sub>2</sub> morning peak (Fig. 5), supporting  
470 traffic/combustion control of the early-day enhancement. In contrast to CO<sub>2</sub>, CO exhibits only a weak mid-  
471 afternoon minimum (including at CH), consistent with CO<sub>2</sub> being additionally depressed by photosynthetic uptake  
472 while CO is unaffected; both species remain modulated by transport and boundary-layer mixing. Weekday–  
473 weekend differences are small at CH but clearer at PY/NS (Fig. S9), indicating a stronger anthropogenic weekly-  
474 cycle imprint in the urban-core and coastal/port settings. Overall, the CO–CO<sub>2</sub> contrast reinforces our interpretation  
475 that the morning CO<sub>2</sub> maxima are primarily combustion-driven, whereas the pronounced mid-afternoon CO<sub>2</sub>  
476 minima at vegetated sites reflect biogenic uptake rather than reduced emissions.

### 477 3.2 Sea–land breeze impacts

478 Based on meteorological observations from the NS coastal tall tower, 84 sea–land breeze days (SLBD) were  
479 identified in Guangzhou between January 2023 and September 2024, accounting for 13.14 % of the monitoring  
480 period, with peaks in spring and autumn. These transitional seasons between summer and winter are characterized  
481 by weaker synoptic systems and lighter background winds, favoring SLBD occurrence (Mai et al., 2024b). Our  
482 results align with SLBD seasonal distributions for the Pearl River Estuary cities of Zhuhai and Guangzhou in 2022  
483 (Zhang et al., 2024; Mai et al., 2024b). Figure 6 compares CO<sub>2</sub> concentrations during SLBD and non-SLB days  
484 (NSLBD) across stations. Overall, average CO<sub>2</sub> concentrations during SLBD were lower than during NSLBD by  
485 5.87 ppm at NS, 3.08 ppm at PY, and 0.75 ppm at CH. This indicates that SLB circulation enhances ventilation and

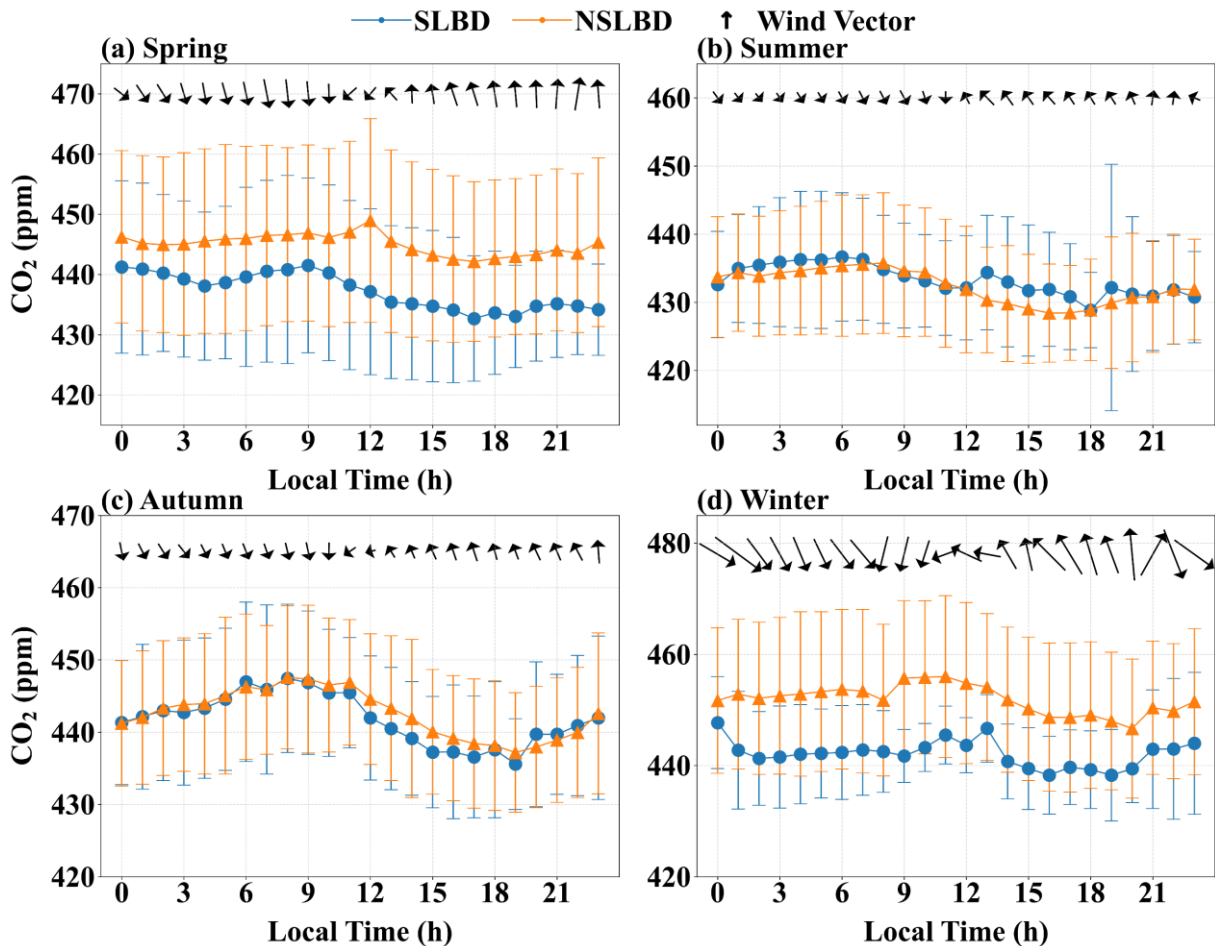
486 CO<sub>2</sub> dispersion, with the SLBD-related reduction decreasing from the coastal site to the urban core and being  
 487 smallest at the suburban site (NS > PY > CH). This pattern is similar to SLB-driven dispersion reported for PM<sub>2.5</sub>,  
 488 PM<sub>10</sub>, and ozone in Tianjin (Hao et al., 2017). Seasonal differences were pronounced: SLB promoted CO<sub>2</sub>  
 489 dispersion at NS and PY in spring, winter, and autumn (spring > winter > autumn), but increased CO<sub>2</sub> accumulation  
 490 in summer. Tianjin similarly observed summer PM<sub>2.5</sub>/PM<sub>10</sub> accumulation under SLB (Hao et al., 2017). At CH,  
 491 SLBD reduced CO<sub>2</sub> in spring, summer, and autumn but increased it in winter, likely due to limited inland SLB  
 492 penetration and competing winter processes.



493  
 494 **Figure 6.** Boxplots of atmospheric CO<sub>2</sub> concentrations (black dots denote means; black lines denote medians) during  
 495 sea–land breeze days (SLBD) and non-SLB days (NSLBD) across seasons (including overall) for the (a) NS, (b) PY, and (c)  
 496 CH stations, with outliers excluded.

497 To resolve seasonal and diurnal SLB impacts, we analyzed CO<sub>2</sub> diurnal variations during SLBD and NSLBD (Fig.

498 7). Focusing on NS (due to similar PY–NS trends and space constraints), spring and winter SLBD reduced CO<sub>2</sub>  
 499 concentrations by 7.76 ppm and 9.77 ppm (hourly mean differences), respectively, driven by stronger winds (Fig.  
 500 7) and deeper boundary layers (Fig. S10 in the Supplement). Autumn SLB only reduced CO<sub>2</sub> during sea breeze  
 501 hours (mean difference: 1.69 ppm). Autumn’s weaker winds and boundary layers resulted in reduced dispersion  
 502 compared to spring/winter. In summer, SLB increased CO<sub>2</sub> by 2.08 ppm (sea breeze hours) due to stable  
 503 atmospheric stratification. Summer temperatures were 6.00 °C and 12.19 °C higher than spring and winter (Table  
 504 S3), respectively. Under calm, rain-free conditions, the collision of moist marine air with dry-hot coastal land  
 505 formed a thermal internal boundary layer (TIBL), inducing low-level temperature inversions near the SLB  
 506 convergence zone (Liu et al., 2001; Reddy et al., 2021). These inversions suppressed horizontal/vertical mixing,  
 507 trapping CO<sub>2</sub> (Stauffer et al., 2015; Hao et al., 2024). NS’s summer SLBD winds averaged 1.05 m s<sup>-1</sup> (sea breeze)  
 508 and 0.96 m s<sup>-1</sup> (land breeze)—38.60 %, 63.16 %, and 15.32 % lower than spring, winter, and autumn winds,  
 509 respectively—while boundary layer heights (590.54 m) were 9.51 % shallower than NSLBD (Fig. S10). Weak  
 510 winds and shallow boundary layers stabilized atmospheric stratification, limiting CO<sub>2</sub> dispersion and elevating  
 511 ground-level CO<sub>2</sub> by up to 4.03 ppm.



512

513

**Figure 7.** Diurnal variations in CO<sub>2</sub> concentrations, wind direction, and wind speed at the coastal station (NS) during

514 sea–land breeze days (SLBD) and non-SLB days (NSLBD) for (a) spring (Mar–May), (b) summer (Jun–Aug), (c) autumn  
515 (Sep–Nov), and (d) winter (Dec–Feb). Error bars indicate  $\pm 1$  SD. The corresponding CO diurnal cycles are shown in Fig.  
516 S11.

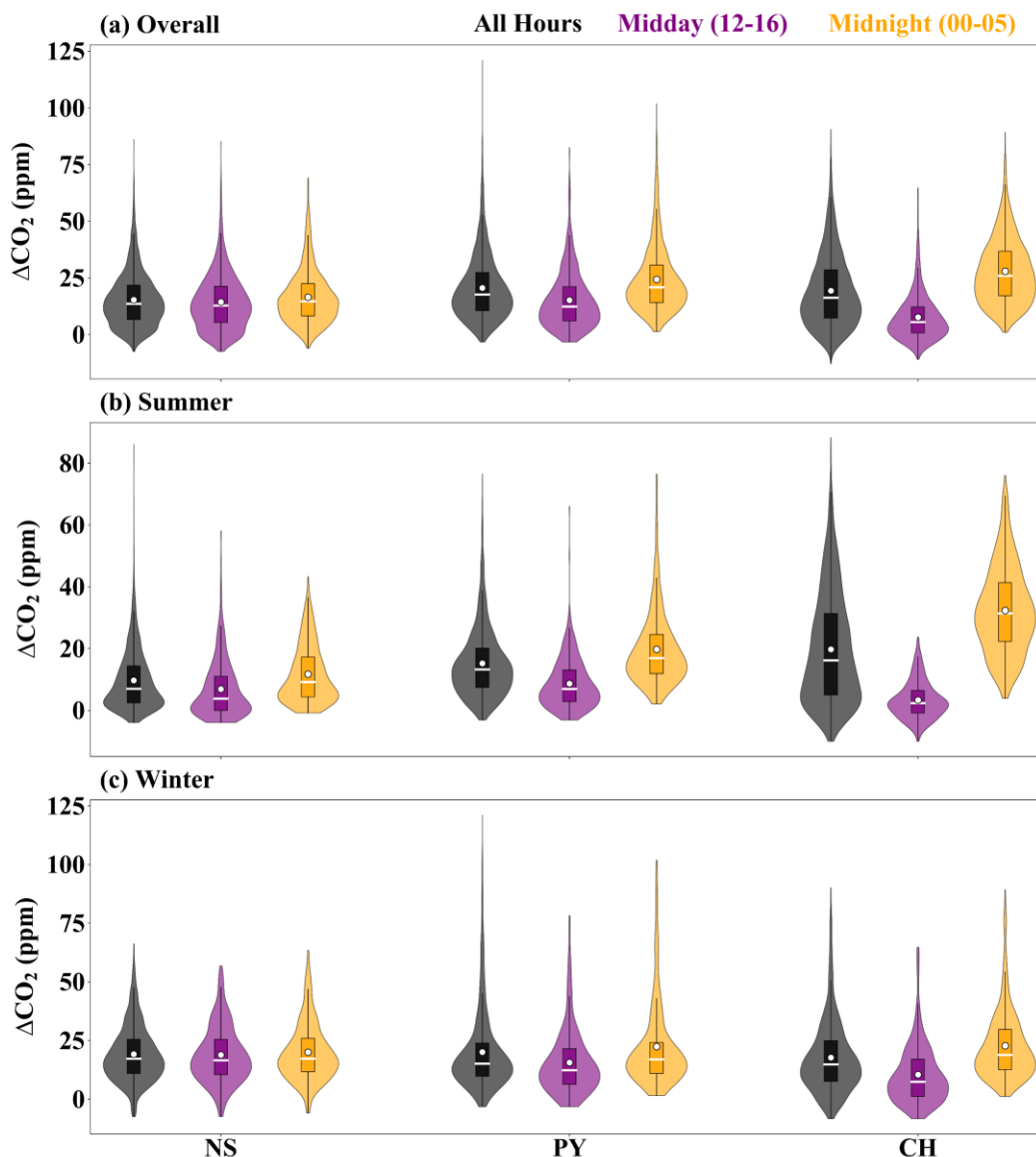
517 CO provides a combustion-specific tracer to further diagnose SLB modulation of anthropogenic signals (Fig. S11  
518 in the Supplement). In spring and winter, CO is generally lower on SLBD than on NSLBD, consistent with  
519 enhanced dilution and export by the breeze circulation, broadly mirroring the CO<sub>2</sub> behavior (Fig. 7). In autumn, the  
520 CO response is weaker and transitional, with only modest daytime reductions. In summer, however, SLB days  
521 exhibit a pronounced afternoon CO build-up, with a much larger relative enhancement than CO<sub>2</sub> (relative to the  
522 seasonal 24 h mean on NSLBD:  $\sim 10$  % for CO versus  $\sim 0.7$  % for CO<sub>2</sub>), implying trapping/recirculation of fresh  
523 combustion plumes under weak-wind, shallow-mixing conditions. Overall, the joint CO–CO<sub>2</sub> behavior confirms  
524 that SLB exerts a seasonally varying control on near-surface carbon signals—ventilating in cooler seasons but  
525 favoring accumulation under the stagnant summer regime.

### 526 3.3 CO<sub>2</sub> enhancements and uncertainties

527 Figure S12 (in the Supplement) presents the time series of observed CO<sub>2</sub> and CO concentrations at Guangzhou’s  
528 stations relative to marine backgrounds from January 1 to December 27, 2023. Compared to urban observations  
529 with significant hourly variability, marine background concentrations in Guangzhou remained stable, with summer  
530 and winter CO<sub>2</sub> standard deviations of 0.94 ppm and 0.67 ppm, respectively, indicating minimal local source/sink  
531 influences. Using Eqs. (13) and (14), marine background uncertainties were calculated (Table S4 in the  
532 Supplement). Summer and winter CO<sub>2</sub> marine background uncertainties were 0.96 ppm and 0.70 ppm, respectively,  
533 constraining urban marine background uncertainties below 1 ppm—slightly lower than Los Angeles’s 1.4 ppm  
534 (Verhulst et al., 2017). CO marine background uncertainties were 12.68 ppb (summer) and 18.36 ppb (winter).

535  
536 Based on background concentrations, CO<sub>2</sub> enhancements were derived for all stations. Figure 8 shows  
537 enhancements across all hours, afternoon (12:00–16:00), and midnight (00:00–05:00) periods in 2023, summer,  
538 and winter. Annual median enhancements were 13.59 (NS), 17.70 (PY), and 16.29 ppm (CH), with pronounced  
539 spatiotemporal variability—closely aligning with the 10–20 ppm range observed annually in the Beijing–Tianjin–  
540 Hebei (BTH) urban cluster of China (Han et al., 2024). In summer, the all-hours enhancement followed a south-to-  
541 north gradient: 7.00 (NS), 13.23 (PY), and 16.91 ppm (CH). This inland maximum likely reflects the combined  
542 influence of coastal transport, biogenic exchange, and boundary-layer mixing, and is consistent with the seasonal  
543 gradient displacement discussed in Sect. 3.1 (Fig. 3). Afternoon enhancements peaked at PY (6.92 ppm), whereas

544 midnight enhancements at CH reached 31.36 ppm. Winter afternoon enhancements reversed this pattern: 16.58  
 545 (NS), 12.37 (PY), and 7.45 ppm (CH), with NS and PY values 4.39 times and 1.79 times higher than summer.  
 546 Midnight enhancements at CH remained highest in winter (18.87 ppm), despite a 38.93 % reduction from summer.



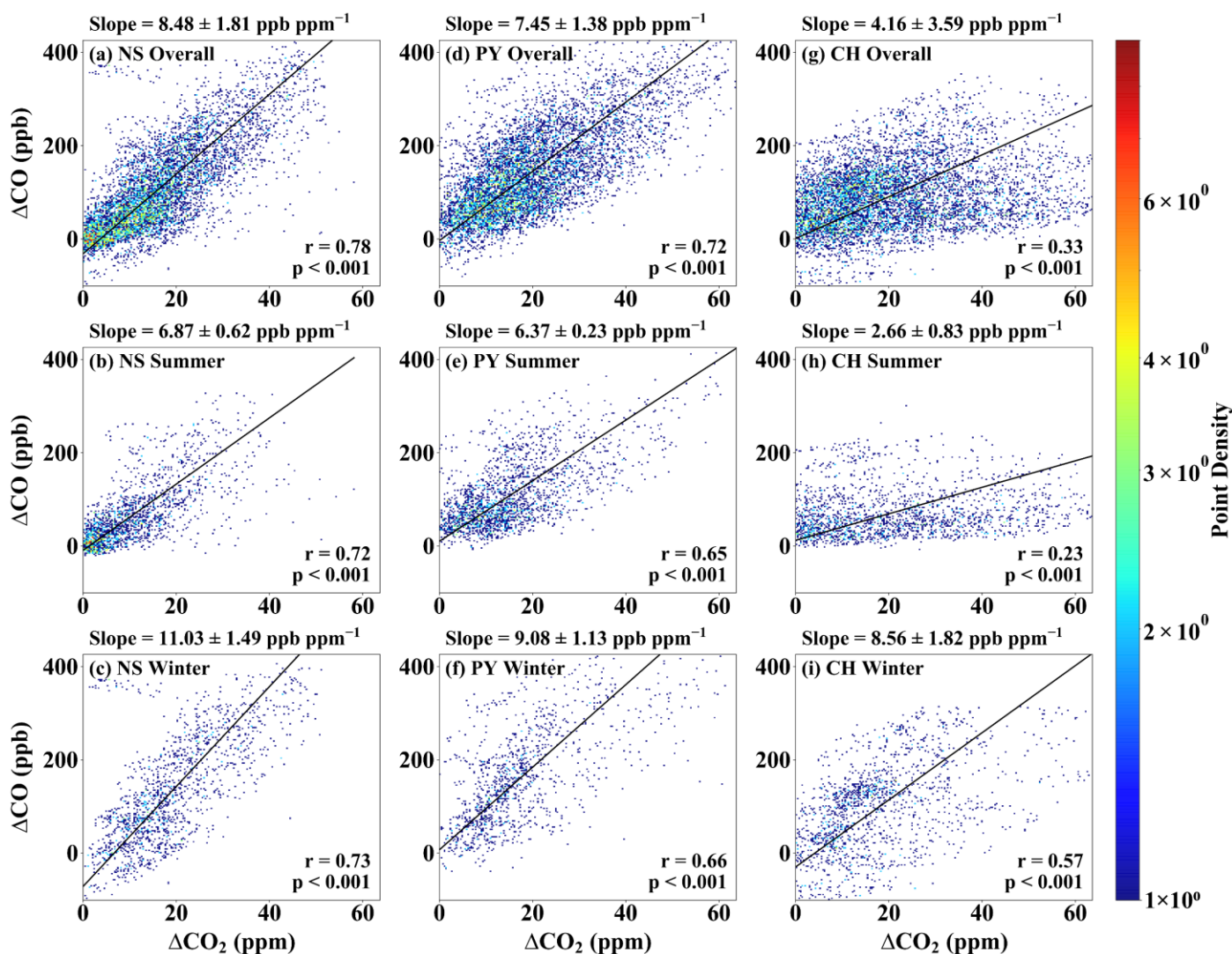
547  
 548 **Figure 8.** Distributions of hourly CO<sub>2</sub> enhancement ( $\Delta\text{CO}_2$ ) above the background concentrations at NS, PY, and CH  
 549 during the (a) overall, (b) summer, and (c) winter periods, shown for all hours, midday (12:00–16:00 LT), and midnight  
 550 (00:00–05:00 LT). White dots denote the mean values, and white horizontal lines denote the median values.

551 This spatiotemporal variability reflects divergent influences of anthropogenic emissions, biogenic fluxes, and  
 552 atmospheric mixing. At CH, strong diurnal shifts in enhancements (e.g., 31.36 ppm summer midnight) highlight  
 553 biogenic dominance, with long-tailed distributions (Fig. 8). Stable, shallow nighttime boundary layers trapped  
 554 respiratory emissions near the surface, consistent with isotopic studies in Xi'an (32.80 ppm) and Switzerland (30.00  
 555 ppm) (Wang et al., 2021; Berhanu et al., 2017). At NS, transport dominated: summer southerly marine air masses  
 556 reduced enhancements, while winter northerly winds transported urban emissions downstream, raising NS

557 enhancements to PY levels (exceeding PY in afternoons). PY's enhancements were primarily anthropogenic,  
 558 validated by CO co-variation. CO, a tracer for combustion-derived CO<sub>2</sub>, showed significantly higher concentrations  
 559 at PY (Fig. S12). PY's median midnight CO enhancements in summer were 2.04 times and 1.43 times higher than  
 560 NS and CH (Fig. S13 in the Supplement). Shallow nocturnal boundary layers localized anthropogenic CO near the  
 561 surface, with minimal vertical/horizontal transport, confirming PY's anthropogenic dominance.

### 562 3.4 Continuous observations of $\Delta\text{CO}/\Delta\text{CO}_2$ ratios

563 Reduced Major Axis regression (Model II) was applied to analyze the relationship between CO ( $\Delta\text{CO}$ ) and CO<sub>2</sub>  
 564 ( $\Delta\text{CO}_2$ ) concentration enhancements across stations, with the  $\Delta\text{CO}/\Delta\text{CO}_2$  emission ratio ( $R_{\text{CO}}$ ) derived from  
 565 regression slopes (Fig. 9). In 2023,  $R_{\text{CO}}$  values for NS, PY, and CH were  $8.48 \pm 1.81$ ,  $7.45 \pm 1.38$ , and  $4.16 \pm 3.59$   
 566 ppb ppm<sup>-1</sup>, respectively, with correlation coefficients of 0.78, 0.72, and 0.33, indicating significant spatiotemporal  
 567 heterogeneity. Summer  $R_{\text{CO}}$  was generally lower than winter, with CH exhibiting the lowest seasonal value ( $2.66 \pm$   
 568  $0.83$  ppb ppm<sup>-1</sup>). Winter maxima occurred at NS ( $11.03 \pm 1.49$  ppb ppm<sup>-1</sup>), followed by PY ( $9.08 \pm 1.13$  ppb ppm<sup>-1</sup>)  
 569 and CH ( $8.56 \pm 1.82$  ppb ppm<sup>-1</sup>).



570

571 **Figure 9.** Seasonal relationships between  $\Delta\text{CO}_2$  and  $\Delta\text{CO}$  enhancements at the (a–c) NS, (d–f) PY, and (g–i) CH stations,  
572 analyzed using geometric-mean regression. Panels are shown as two-dimensional (2-D) histogram density plots (hist2d; 200  
573  $\times$  200 bins), where color indicates the number of paired observations per bin. The fitted slope represents the  $\Delta\text{CO}/\Delta\text{CO}_2$   
574 emission ratio ( $R_{\text{CO}}$ ; ppb ppm<sup>-1</sup>), reported as mean  $\pm$  1 SD (reflecting temporal variability).

575 Comparatively, Beijing’s urban  $R_{\text{CO}}$  in 2019 was measured at  $10.46 \pm 0.11$  ppb ppm<sup>-1</sup> using portable Fourier-  
576 transform spectroscopy (Che et al., 2022a), while Shanghai and Los Angeles showed  $10.22 \pm 0.40$  and  $9.64 \pm 0.46$   
577 ppb ppm<sup>-1</sup>, respectively, based on satellite and model data (Wu et al., 2022a). Guangzhou’s lower  $R_{\text{CO}}$  is consistent  
578 with the post-2013 tightening of China’s air-quality management across the energy and transport sectors, rather  
579 than a single intervention. National action plans (2013–2017 Air Pollution Prevention and Control Action Plan;  
580 2018–2020 Three-Year “Blue-Sky” Action Plan) strengthened coal/industrial and vehicle-emission controls with  
581 explicit targets and timelines. In parallel, ultra-low-emission (ULE) retrofits of coal-fired power units were rolled  
582 out through 2020, and China 6 (VI) on-road emission standards were phased in, with large cities (including  
583 Guangzhou) leading implementation; Guangdong’s provincial Blue-Sky measures further reinforced  
584 industrial/mobile-source controls and promoted fleet electrification. These measures coincide with independent  
585 inventory evidence of declining national CO emissions ( $\sim 23\%$  during 2013–2017) (Zheng et al., 2018), plausibly  
586 reducing CO/CO<sub>2</sub> emission ratios from dominant urban sources. Consistently, Beijing’s  $R_{\text{CO}}$  decreased from  $> 30$   
587 ppb ppm<sup>-1</sup> in 2006 (Han et al., 2009) to  $10.22 \pm 0.40$  ppb ppm<sup>-1</sup> by 2020 (Wu et al., 2022a), with additional  
588 reductions during the 2008 Olympics and 2020 COVID-19 lockdowns (Wang et al., 2010; Cai et al., 2021). In  
589 Guangdong, restrictions on coal plants, retirement of inefficient industries, and promotion of electric vehicles  
590 coincided with large declines in SO<sub>2</sub> and NO<sub>2</sub> (85% and 35% in 2019 relative to 2006) (Hu et al., 2021), and Mai  
591 et al. (2021) likewise reported improved combustion efficiency in the PRD associated with advances in gasoline  
592 vehicles. We emphasize that this interpretation is consistency-based rather than a formal causal identification; fuel  
593 mix, fleet composition, and atmospheric oxidation may also contribute (Young et al., 2023; Vimont et al., 2019).

594  
595 Seasonal  $R_{\text{CO}}$  variations stem from biogenic exchange and transport dynamics. Summer’s weaker  $\Delta\text{CO}$ – $\Delta\text{CO}_2$   
596 correlations at CH reflect dominant biogenic influences (daytime uptake and nighttime respiration), as reported in  
597 Beijing, Indianapolis, and Switzerland (Turnbull et al., 2015; Berhanu et al., 2017; Che et al., 2022a). Biogenic  
598 impacts decreased from suburban  $>$  urban  $>$  coastal, aligning with vegetation gradients. Winter’s higher  $R_{\text{CO}}$  at CH  
599 and NS correlated with reduced biogenic activity and northerly transport of urban emissions under stable boundary  
600 layers. Berhanu et al. (2017) attributed winter  $R_{\text{CO}}$  increases to cold-air advection and boundary layer accumulation.  
601 NS’s winter  $R_{\text{CO}}$  ( $4.16$  ppb ppm<sup>-1</sup> higher than summer) linked to urban air mass origins, while PY’s seasonal shifts  
602 reflected suburban source–sink variations. Although secondary CO from upwind Volatile Organic Compounds

603 (VOCs) and Methane (CH<sub>4</sub>) oxidation could perturb R<sub>CO</sub>, their combined contribution was merely 1 % in coastal  
604 urban regions (Griffin et al., 2007).

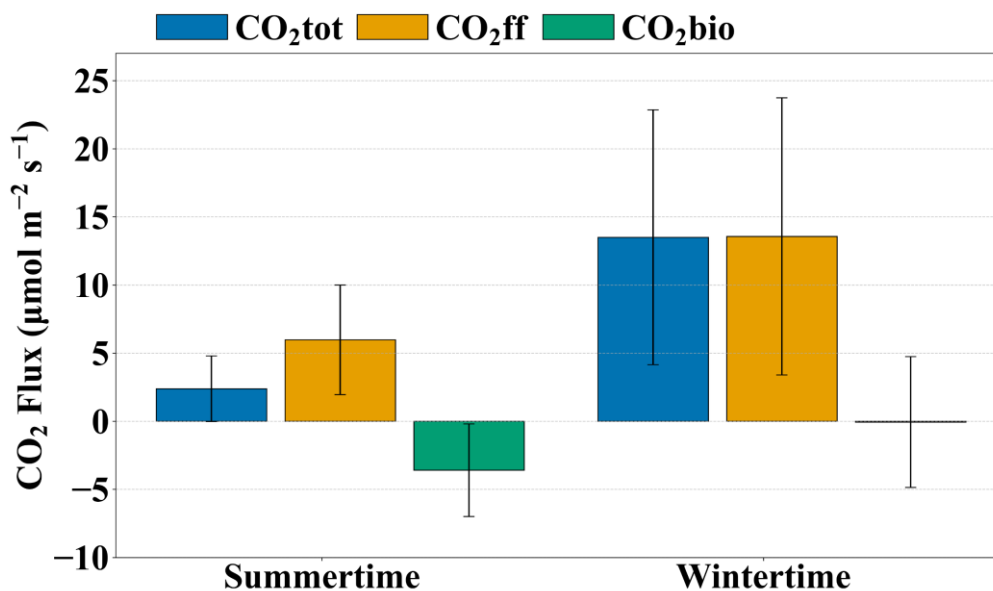
### 605 **3.5 Partitioning anthropogenic and biogenic fluxes**

606 Section 3.4 shows that the sites differ in how well the  $\Delta\text{CO}-\Delta\text{CO}_2$  relationship reflects fossil-fuel combustion. At  
607 CH, especially in summer, CO<sub>2</sub> variability is strongly influenced by biogenic exchange, which weakens the  
608 combustion linkage implied by R<sub>CO</sub> and can bias an R<sub>CO</sub>-based fossil-fuel estimate. At NS, in contrast, variability  
609 is dominated by changing transport and upwind air mass origin, particularly in winter when urban plumes frequently  
610 reach the coastal site. We therefore select PY—the urban-core site with a comparatively robust combustion signal—  
611 to quantify the surface CO<sub>2</sub> emissions (CO<sub>2</sub>tot) constrained by the observed concentration enhancements and  
612 footprint-informed transport. Using the PY-specific R<sub>CO</sub>, we then partition CO<sub>2</sub>tot into fossil-fuel (CO<sub>2</sub>ff) and  
613 biogenic (CO<sub>2</sub>bio) components.

614

615 Figure 10 summarizes mean afternoon (12:00–16:00 LT) CO<sub>2</sub>tot, CO<sub>2</sub>ff, and CO<sub>2</sub>bio at PY for July 2023 (summer)  
616 and December 2023 (winter). Bars show monthly means of daily afternoon values. The plotted error bars indicate  
617  $\pm 1$  standard deviation (SD) across days and thus represent day-to-day variability in ventilation, mixing, and  
618 transport rather than uncertainty of the monthly mean. Mean uncertainty is quantified by the standard error (SE),  
619 which is distinct from the SD shown in Fig. 10. In July, CO<sub>2</sub>tot =  $2.38 \pm 0.45$ , CO<sub>2</sub>ff =  $5.97 \pm 0.75$ , and CO<sub>2</sub>bio =  
620  $-3.59 \pm 0.63 \mu\text{mol m}^{-2} \text{s}^{-1}$  (mean  $\pm$  SE), whereas in December CO<sub>2</sub>tot =  $13.50 \pm 2.20$ , CO<sub>2</sub>ff =  $13.56 \pm 2.40$ , and  
621 CO<sub>2</sub>bio =  $-0.06 \pm 1.13 \mu\text{mol m}^{-2} \text{s}^{-1}$  (Table S5). Because CO<sub>2</sub>bio is diagnosed as a residual (CO<sub>2</sub>bio = CO<sub>2</sub>tot –  
622 CO<sub>2</sub>ff), its uncertainty reflects propagated uncertainties from both CO<sub>2</sub>tot and CO<sub>2</sub>ff—including measurement and  
623 background-selection uncertainty and R<sub>CO</sub>-related variability—rather than being independent. Notably, December  
624 CO<sub>2</sub>bio is close to zero. The bootstrap 95 % CI of the monthly mean is  $[-2.28, 2.09] \mu\text{mol m}^{-2} \text{s}^{-1}$ , which includes  
625 zero, indicating that the net biogenic flux was not statistically distinguishable from zero during winter afternoons,  
626 likely reflecting a near-neutral balance between photosynthesis and respiration. In contrast, the July mean CO<sub>2</sub>bio  
627 remains clearly negative relative to its uncertainty, supporting robust summertime net biogenic uptake despite  
628 uncertainty propagation inherent to the residual calculation. When assessed using daily afternoon means, the July–  
629 December contrasts are statistically significant for CO<sub>2</sub>tot, CO<sub>2</sub>ff, and CO<sub>2</sub>bio (Welch and Mann–Whitney tests;  
630 bootstrap 95 % confidence intervals; Table S5). Robust distributional metrics corroborate this significant seasonal  
631 increase despite partial day-to-day overlap: the CO<sub>2</sub>ff median increases from 4.33 (IQR: 3.58–7.81) in July to 10.70  
632 (IQR: 6.74–18.28)  $\mu\text{mol m}^{-2} \text{s}^{-1}$  in December. Across both months, CO<sub>2</sub>ff is larger in magnitude than CO<sub>2</sub>bio,

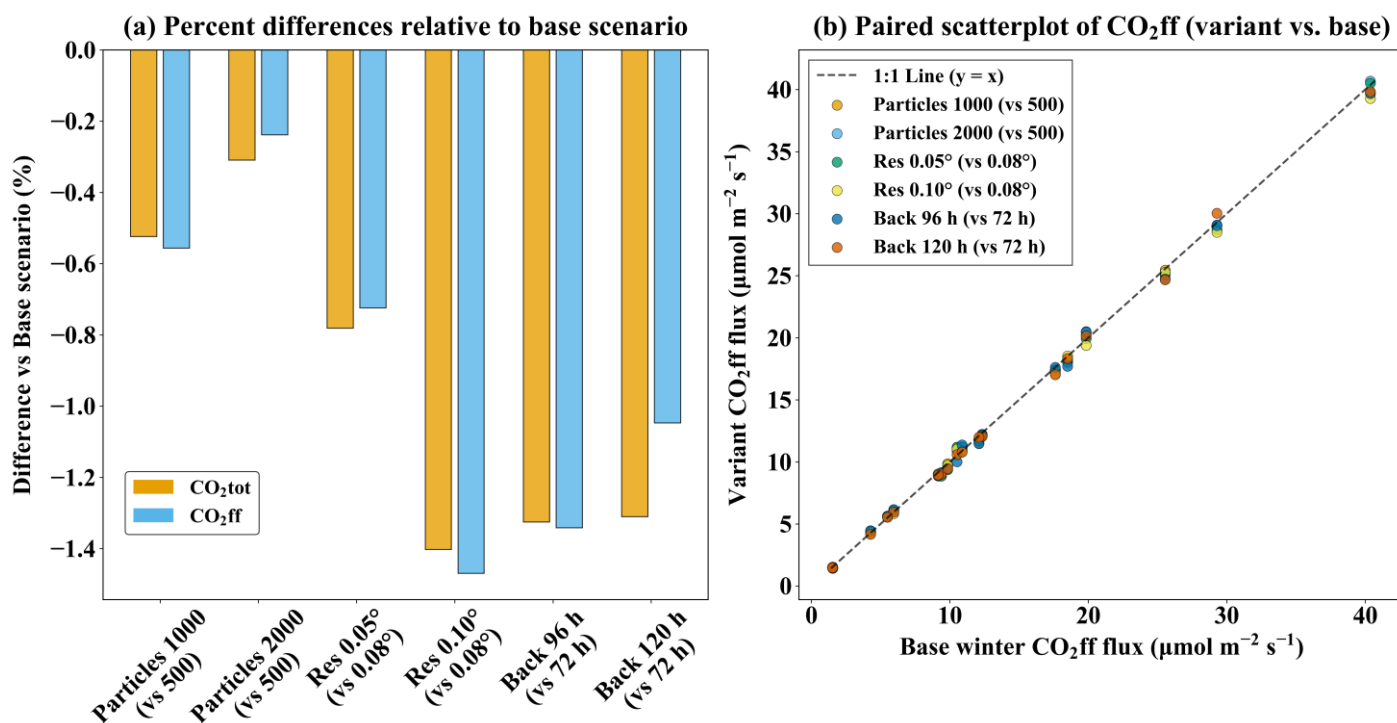
633 implying that the PY afternoon enhancement is primarily fossil-fuel driven, consistent with fossil-dominated urban  
 634 enhancements reported for other Chinese cities (Wang et al., 2022). The stronger winter CO<sub>2</sub>ff relative to summer  
 635 is explained mainly by atmospheric dynamics—reduced dilution under weaker marine ventilation and a shallower  
 636 boundary layer—while seasonal emission changes (e.g., winter residential energy use) likely provide a secondary  
 637 contribution. In contrast, CO<sub>2</sub>bio is more negative in summer, consistent with higher summer NDVI (+11 %) and  
 638 warmer conditions approaching optimal canopy temperatures (Table S3).



639 **Figure 10.** Average afternoon (12:00–16:00 LT) CO<sub>2</sub>tot, CO<sub>2</sub>ff, and CO<sub>2</sub>bio at PY for July 2023 (summer; n = 29 valid  
 640 days) and December 2023 (winter; n = 18 valid days). December has fewer valid days because objective QC excluded days  
 641 with incomplete afternoon coverage (e.g., instrument downtime/maintenance), so the smaller winter sample reflects data  
 642 availability rather than subjective selection. Bars show monthly means of daily afternoon values. Error bars indicate ± 1 SD  
 643 across daily afternoon means within each month (day-to-day atmospheric variability), not the SE of the monthly mean; SE  
 644 and confidence intervals are reported in Table S5.

646 To test the robustness of the winter fossil-fuel dominance inferred at PY—when combustion signals are strongest—  
 647 we reran the winter flux-estimation workflow using paired daily afternoon means (12:00–16:00 LT). We then varied  
 648 (1) particle number (1000/2000), (2) grid spacing (0.05°/0.10°), and (3) backward duration (96/120 h) relative to  
 649 the baseline (500 particles, 0.08°, 72 h). Mean changes were small for both components (Table S6 in the Supplement;  
 650 Fig. 11a). Increasing particle number to 1000/2000 changed CO<sub>2</sub>ff by –0.56 %/–0.24 % and CO<sub>2</sub>tot by  
 651 –0.52 %/–0.31 %. Refining the grid to 0.05° yielded comparably small decreases (CO<sub>2</sub>ff: –0.72 %; CO<sub>2</sub>tot:  
 652 –0.78 %). Extending the backward duration to 96/120 h produced changes of –1.34 %/–1.05 % for CO<sub>2</sub>ff and  
 653 –1.33 %/–1.31 % for CO<sub>2</sub>tot. Only the coarser 0.10° grid produced a statistically detectable, yet small, decrease  
 654 (CO<sub>2</sub>ff: –1.47 %, p = 0.0269; CO<sub>2</sub>tot: –1.40 %, p = 0.0164). All other settings yielded changes ≤ 1.34 % with 95 %  
 655 CIs spanning zero (p ≥ 0.083), indicating no evidence of material bias at our sample size. Day-to-day consistency

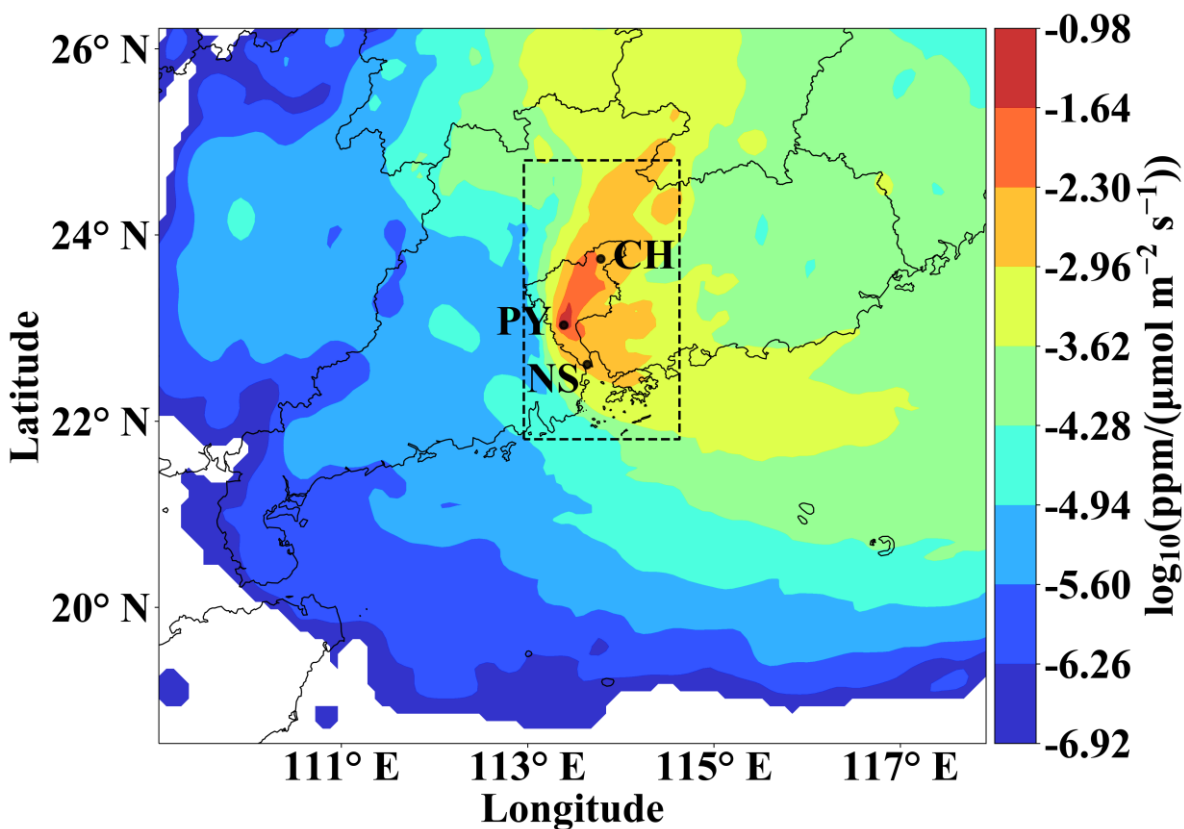
656 remained essentially unchanged across settings, with extremely high correlations ( $\text{CO}_2\text{ff}$ :  $r = 0.9993\text{--}0.9997$ ;  
 657  $\text{CO}_2\text{tot}$ :  $r = 0.9992\text{--}0.9997$ ) and small RMSE values ( $\text{CO}_2\text{ff}$ :  $0.31\text{--}0.45 \mu\text{mol m}^{-2} \text{s}^{-1}$ ;  $\text{CO}_2\text{tot}$ :  $0.28\text{--}0.45 \mu\text{mol m}^{-2}$   
 658  $\text{s}^{-1}$ ), consistent with the near-1:1 paired scatter (Fig. 11b). Because wintertime  $\text{CO}_2\text{bio}$  at PY was close to zero,  
 659 percent differences were not informative; in absolute terms, test–baseline differences in  $\text{CO}_2\text{bio}$  remained small  
 660 (order  $10^{-2} \mu\text{mol m}^{-2} \text{s}^{-1}$ ) with 95 % CIs generally spanning zero, consistent with the tight across-run daily spread  
 661 (median  $0.045 \mu\text{mol m}^{-2} \text{s}^{-1}$ ; IQR  $0.016\text{--}0.067 \mu\text{mol m}^{-2} \text{s}^{-1}$ ) (Table S7 in the Supplement). Across the baseline  
 662 plus six variants, the day-by-day ensemble spread was tightly bounded (median  $0.20\text{--}0.21 \mu\text{mol m}^{-2} \text{s}^{-1}$ , median  
 663  $\text{CV} \approx 1.8\%$ ). Together, these results indicate that our baseline STILT configuration lies in a converged regime and  
 664 that the inferred winter  $\text{CO}_2\text{ff}$  dominance is robust to reasonable transport-parameter choices.



665  
 666 **Figure 11.** STILT parameter sensitivity at PY (winter). **(a)** Mean percent difference (variant – baseline) of inferred fluxes  
 667 relative to the winter baseline (500 particles,  $0.08^\circ$ , 72 h), computed from paired daily afternoon means (12:00–16:00 LT;  $n =$   
 668 18);  $\Delta\% = (\text{variant} - \text{base}) / \text{base} \times 100$ ; negative values indicate lower than baseline. **(b)** Paired scatter of  $\text{CO}_2\text{ff}$  ( $\mu\text{mol m}^{-2}$   
 669  $\text{s}^{-1}$ ) from each variant versus the baseline for the same days; solid line is 1:1 ( $y = x$ ).

670 For winter afternoons at PY, measurement and background-selection uncertainties—estimated by propagating their  
 671 combined enhancement uncertainty through Eqs. (12)–(14)—contribute only  $\sim 0.36 \mu\text{mol m}^{-2} \text{s}^{-1}$ , i.e.,  $\sim 3\%$  of  
 672 the mean winter-afternoon  $\text{CO}_2\text{ff}$ . Paired-day STILT sensitivity tests (Fig. 11) further indicate that the winter-  
 673 afternoon  $\text{CO}_2\text{ff}$  attribution is robust to reasonable transport-parameter choices. The remaining uncertainty is thus  
 674 more likely dominated by residual transport representation error and coastal mesoscale flow (e.g., wind and  
 675 boundary-layer mixing biases), as documented for winter conditions in meteorological/transport modeling (Yadav  
 676 et al., 2021; Lin et al., 2021). To provide independent context, we benchmark our winter-afternoon estimate against

677 bottom-up inventories, which are used solely for contextual comparison and do not enter the CO<sub>2</sub> partitioning. We  
 678 use 2023 inventories at 0.1° × 0.1° resolution, temporally disaggregate annual totals to hourly emissions using the  
 679 same profiles (Crippa et al., 2020), and compute the winter-afternoon (12:00–16:00 LT) mean emission flux over  
 680 the winter footprint-defined sensitivity region (Fig. 12). This yields 19.81 μmol m<sup>-2</sup> s<sup>-1</sup> from the  
 681 EDGAR\_2024\_GHG (2023) inventory (Crippa et al., 2024) and 85.46 μmol m<sup>-2</sup> s<sup>-1</sup> from the MEIC-global-CO<sub>2</sub>  
 682 (2023) inventory (Xu et al., 2024). While this aligns qualitatively with higher MEIC estimates reported for  
 683 Guangdong Province (Yang et al., 2025), the contrast is larger for our winter-afternoon sensitivity region. This  
 684 likely reflects differences in spatial disaggregation and point-source representation (e.g., road-network allocation  
 685 and power-plant locations) that can be accentuated at sub-provincial scales (Yang et al., 2025).



686  
 687 **Figure 12.** Spatial distribution of the mean winter-afternoon (12:00–16:00 LT) STILT footprint at the PY station,  
 688 representing the receptor sensitivity to upwind surface fluxes. Colors denote the log<sub>10</sub>-transformed footprint sensitivity (ppm  
 689 / (μmol m<sup>-2</sup> s<sup>-1</sup>)). The dashed rectangle outlines the sensitivity region used for inventory flux aggregation and benchmarking  
 690 in Sect. 3.5.

691 Notably, our observation-based CO<sub>2</sub>ff reflects the footprint-weighted enhancement sampled at PY during winter  
 692 afternoons after background removal, whereas inventories provide gridded emission fields from which an  
 693 unweighted domain-mean afternoon flux can be computed over the sensitivity region. Because only grid cells with  
 694 substantial STILT footprint influence contribute materially to the receptor enhancement—and these weights are  
 695 highly heterogeneous and transport-dependent (Fig. 12)—the unweighted domain-mean inventory flux may be non-

696 uniformly represented in the receptor signal under variable coastal transport (Gerbig et al., 2003; Lin et al., 2003;  
697 Fasoli et al., 2018). Accordingly, an effective footprint-weighted mean flux estimate inferred from the receptor  
698 enhancement can differ from the unweighted afternoon-mean inventory flux over the sensitivity region. This  
699 difference depends on the spatial alignment between heterogeneous transport footprints and spatially heterogeneous  
700 emissions (including localized hotspots), because under a given transport regime many grid cells within the domain  
701 may carry negligible footprint influence (Hüser et al., 2017; Kunik et al., 2019). We therefore interpret inventory  
702 comparisons as a plausibility envelope that reflects inter-inventory spread, rather than a validation target. Such  
703 inventory–observation differences are also reported for other coastal urban basins (e.g., Los Angeles) and are often  
704 sensitive to boundary-layer representation and meteorological inputs (Kim et al., 2025).

705

706 Beyond the winter fossil-fuel benchmark above, we further place the summer biogenic component and its offset  
707 ratio in the context of independent regional and urban estimates. Summer afternoons exhibited mean  $\text{CO}_2^{\text{bio}}$  of  
708  $-3.59 \pm 0.63 \mu\text{mol m}^{-2} \text{s}^{-1}$ , consistent with observation-based Pearl River Delta NEE ( $-0.1$  to  $-12 \mu\text{mol m}^{-2} \text{s}^{-1}$ )  
709 (Mai et al., 2024a), and with modeled urban biogenic flux ranges (0 to  $-15 \mu\text{mol m}^{-2} \text{s}^{-1}$ ) reported in previous  
710 studies (Wu et al., 2021; Wei et al., 2022; Kim et al., 2025). Consequently, summer-afternoon biogenic uptake  
711 offsets 60.13 % of concurrent  $\text{CO}_2^{\text{ff}}$  at PY, with a bootstrap 95 % confidence interval of 48–72 %, highlighting  
712 substantial biogenic modulation of coastal urban  $\text{CO}_2$  signals. Importantly, the inferred summertime offset remains  
713 substantial within the estimated uncertainty range, indicating robust biogenic modulation in magnitude.  
714 Comparable growing-season offsets have been reported for other coastal urban regions using independent  
715 approaches. A sensor-network combined with box-model analysis for Los Angeles suggests up to 60 % daytime  
716 offset; an inversion for the Boston coastal region indicates  $> 50$  % summer-afternoon offset (Kim et al., 2025;  
717 Sargent et al., 2018). High-resolution vegetation modeling for New York City similarly suggests  $\sim 40$  % offset of  
718 afternoon anthropogenic enhancements and the potential to fully balance on-road traffic contributions (Wei et al.,  
719 2022). Overall, these contextual comparisons provide an external plausibility check and indicate that strong  
720 growing-season biogenic uptake is a plausible and important modulator of coastal-urban  $\text{CO}_2$  signals in Guangzhou.

## 721 4 Conclusions

722 ~~Three key knowledge gaps still limit the interpretation of atmospheric  $\text{CO}_2$  signals in coastal megacities and their~~  
723 ~~use for mitigation-relevant assessment. To address them, We develop~~ an observation-driven framework to interpret  
724 coastal megacity  $\text{CO}_2$  dynamics in Guangzhou (January 2023–September 2024) using multi-site  $\text{CO}_2/\text{CO}$   
725 measurements, footprint-informed transport analysis, and a site-specific  $\Delta\text{CO}/\Delta\text{CO}_2$  ( $R_{\text{CO}}$ ) relationship, without

726 assimilating emission inventories. ~~Relative to prior studies, this framework provides a distinct, process-based view~~  
727 ~~of spatiotemporal CO<sub>2</sub> variability, sea-land breeze (SLB) modulation, and source-sink partitioning in a coastal~~  
728 ~~setting.~~ The three-site gradient reveals contrasting dominant controls by setting: transport governs the largest  
729 seasonal amplitude at the coastal site, biogenic exchange drives pronounced summertime daytime drawdown at the  
730 vegetated site, and combustion dominates variability in the urban core. This combustion signal is characterized by  
731 a regression-derived R<sub>CO</sub>, ~~broadly consistent with a regional shift toward cleaner fuels and stricter vehicle-emission~~  
732 ~~controls.~~ Importantly, these patterns point to a seasonally displaced “coastal CO<sub>2</sub> dome”. In contrast to the  
733 traditional paradigm ~~in which~~ the maximum CO<sub>2</sub> enhancement is anchored over the urban center, our results ~~show~~  
734 that ~~in coastal megacities~~ the dome’s peak can ~~shift away~~ from the urban core. ~~This shift reflects~~ the combined  
735 effects of seasonal coastal transport/mixing and seasonally varying biogenic ~~exchange~~ associated with urban  
736 greening, underscoring the dynamic nature of coastal greenhouse gas distributions.

737

738 Under prevailing fair-weather coastal mesoscale conditions, the SLB circulation exerts a key control on diurnal  
739 variability in near-surface CO<sub>2</sub> and CO, with a non-linear seasonal modulation. In spring and winter, SLB  
740 strengthens ventilation and lowers CO<sub>2</sub>, whereas in summer it can favor accumulation ~~(+2.08 ppm during sea-~~  
741 ~~breeze hours)~~ under weak-wind, stable conditions. Consistent with this, CO exhibits a more pronounced daytime  
742 enhancement than CO<sub>2</sub> during SLB days ~~in summer~~, supporting a trapping/recirculation regime in which  
743 combustion plumes are retained when coastal mesoscale flows coincide with shallow mixing and stable  
744 stratification. These seasonally opposing SLB impacts may be overlooked because many urban CO<sub>2</sub> studies focus  
745 on inland settings or annual-mean signals. Our results show that coastal mesoscale circulations can reverse the sign  
746 of SLB effects across seasons, highlighting important implications for inversion design and interpretation in coastal  
747 cities.

748

749 Source-sink attribution at PY indicates that winter-afternoon CO<sub>2</sub>ff ~~estimates are robust to measurement~~  
750 ~~uncertainty and background selection, with only minor sensitivity to the tested transport-model configurations. This~~  
751 ~~supports the reliability of our framework for this coastal megacity setting under the adopted sampling and~~  
752 ~~background definition.~~ In summer afternoons, inferred CO<sub>2</sub>bio ~~(-3.59 ± 0.63 μmol m<sup>-2</sup> s<sup>-1</sup>)~~ shows substantial  
753 biogenic uptake that offsets ~ 60 % of the concurrent CO<sub>2</sub>ff during the peak growing season, ~~and this offset remains~~  
754 ~~substantial within the estimated uncertainty bounds.~~ This summertime offset ~~aligns with~~ independent estimates for  
755 other coastal urban regions, ~~supporting the~~ plausibility of our source-sink separation ~~and suggesting that strong~~  
756 ~~biogenic modulation can persist even under complex SLB-driven coastal transport.~~

757

758 Several limitations remain. The three-site network cannot resolve hyperlocal source heterogeneity, and SLB  
759 identification relies on near-surface wind criteria rather than [the full 3-D boundary-layer structure](#). Although  
760 configuration sensitivity is small, transport uncertainties associated with winds and boundary-layer mixing are not  
761 fully quantified here. In addition, CO-based attribution is sensitive to variability in  $R_{CO}$  arising from changing  
762 source mix, plume processing, and background definition, which propagates into [inferred  \$CO\_2^{ff}\$](#)  and the residual  
763  $CO_2^{bio}$ . Future work combining denser low-cost networks, boundary-layer profiling, and periodic isotopic  
764 constraints would further tighten coastal urban carbon budgets.

765

766 Overall, coastal mesoscale dynamics can [invert the seasonal role of SLB—from ventilation in cool seasons to](#)  
767 [trapping/recirculation in summer—thereby reshaping urban  \$CO\_2\$  signals in coastal megacities](#). Meanwhile, a  
768 substantial summertime biogenic offset associated with urban greening can [strongly damp](#) apparent fossil-fuel  
769 signals and should be [considered when evaluating](#) mitigation trends. These findings have direct implications for  
770 coastal urban monitoring and policy evaluation: to avoid season-dependent biases in assessing mitigation progress,  
771 urban monitoring networks should prioritize the decoupling of biogenic signals—particularly during summer—to  
772 accurately isolate anthropogenic contributions and thus ensure [reliable](#) evaluation of mitigation progress.  
773 Furthermore, the strategic selection of monitoring sites in coastal megacities must explicitly account for the non-  
774 linear accumulation effects of SLB circulations to ensure long-term sampling representativeness. While our  
775 framework does not produce posterior flux fields as in a formal Bayesian inversion, it provides a complementary,  
776 observation-driven tool for rapid process attribution and consistency checking in coastal urban carbon monitoring  
777 and mitigation assessment.

778 **Code and data availability.** The STILT model source code used in this paper has been published on Zenodo and  
779 can be accessed at <https://doi.org/10.5281/zenodo.1196561> (Fasoli, 2018). The EDGAR data used in this study are  
780 publicly available at [https://edgar.jrc.ec.europa.eu/dataset\\_ghg2024#conditions](https://edgar.jrc.ec.europa.eu/dataset_ghg2024#conditions) (last access: 18 June 2025)(Crippa  
781 et al., 2024). The planetary boundary layer height data used in this study are available at  
782 <https://doi.org/10.24381/cds.adbb2d47> (Hersbach, 2023). The NDVI data used in this study are available at  
783 <https://doi.org/10.5067/MODIS/MOD13A3.006> (Didan, 2015). The CarbonTracker (CT-NRT.v2024-5) products  
784 are available online at <https://doi.org/10.15138/ATPD-K925> (Jacobson et al., 2024). The NOAA Earth System  
785 Research Laboratory/Global Monitoring Laboratory (NOAA GML) data used in this study are available at  
786 <https://doi.org/10.25925/20241101> (Schuldt et al., 2024). Additional data and information used in this study are  
787 available from the corresponding author upon request.

788 **Author contributions.** JWZ and ML designed the study. JWZ, YJL, CLP, BH, YYH, XFL, SJS, CLC, CW, ZZ,  
789 JJJ and ML contributed to data collection and data analysis. JWZ designed and performed the model simulations.

790 JWZ and ML wrote the paper with contributions from all coauthors. JJL and SJS provided valuable feedback and  
791 opinions for paper refinement. All the authors revised the paper and edited the text.

792 **Competing interests.** The contact author has declared that none of the authors has any competing interests.

793 **Disclaimer.** Publisher's note: ~~Publisher's note:~~ Copernicus Publications remains neutral with regard to  
794 jurisdictional claims in published maps and institutional affiliations.

795 **Acknowledgements.** The authors would like to thank the personnel who participated in data collection, instrument  
796 maintenance, and logistic support during the field campaign. We also acknowledge the NOAA GML for providing  
797 the CO<sub>2</sub> GLOBALVIEWplus v10.1 ObsPack and CarbonTracker CT-NRT.v2024-5 datasets, which were used for  
798 monitoring comparison in this study. CarbonTracker CT-NRT.v2024-5 results provided by NOAA GML, Boulder,  
799 Colorado, USA from the website at <http://carbontracker.noaa.gov>.

800 **Financial support.** This work was financially supported by the National Natural Science Foundation of China  
801 (Grant no. 42477273) and the National Key R&D Program of China (Grant no. 2022YFE0209500).

## 802 References

- 803 Ahmadov, R., Gerbig, C., Kretschmer, R., Koerner, S., Neining, B., Dolman, A., and Sarrat, C.: Mesoscale covariance of  
804 transport and CO<sub>2</sub> fluxes: Evidence from observations and simulations using the WRF - VPRM coupled atmosphere -  
805 biosphere model, *J. Geophys. Res.-Atmos.*, 112, <https://doi.org/10.1029/2007JD008552>, 2007.
- 806 Allouche, M., Bou - Zeid, E., and Iipponen, J.: The influence of synoptic wind on land - sea breezes, *Quarterly Journal of the*  
807 *Royal Meteorological Society*, 149, 3198-3219, <https://doi.org/10.1002/qj.4552>, 2023.
- 808 Atkins, N. T. and Wakimoto, R. M.: Influence of the synoptic-scale flow on sea breezes observed during CaPE, *Monthly*  
809 *weather review*, 125, 2112-2130, [https://doi.org/10.1175/1520-0493\(1997\)125<2112:IOTSSF>2.0.CO;2](https://doi.org/10.1175/1520-0493(1997)125<2112:IOTSSF>2.0.CO;2), 1997.
- 810 Berhanu, T. A., Szidat, S., Brunner, D., Satar, E., Schanda, R., Nyfeler, P., Battaglia, M., Steinbacher, M., Hammer, S., and  
811 Leuenberger, M.: Estimation of the fossil fuel component in atmospheric CO<sub>2</sub> based on radiocarbon measurements at the  
812 Beromünster tall tower, Switzerland, *Atmos. Chem. Phys.*, 17, 10753-10766, <https://doi.org/10.5194/acp-17-10753-2017>,  
813 2017.
- 814 Boon, A., Broquet, G., Clifford, D. J., Chevallier, F., Butterfield, D. M., Pison, I., Ramonet, M., Paris, J.-D., and Ciais, P.:  
815 Analysis of the potential of near-ground measurements of CO<sub>2</sub> and CH<sub>4</sub> in London, UK, for the monitoring of city-scale  
816 emissions using an atmospheric transport model, *Atmos. Chem. Phys.*, 16, 6735-6756, [https://doi.org/10.5194/acp-16-6735-](https://doi.org/10.5194/acp-16-6735-2016)  
817 [2016](https://doi.org/10.5194/acp-16-6735-2016), 2016.
- 818 Briber, B. M., Hutyra, L. R., Dunn, A. L., Raciti, S. M., and Munger, J. W.: Variations in atmospheric CO<sub>2</sub> mixing ratios across  
819 a Boston, MA urban to rural gradient, *Land*, 2, 304-327, <https://doi.org/10.3390/land2030304>, 2013.
- 820 Cai, Z., Che, K., Liu, Y., Yang, D., Liu, C., and Yue, X.: Decreased anthropogenic CO<sub>2</sub> emissions during the COVID-19  
821 pandemic estimated from FTS and MAX-DOAS measurements at urban Beijing, *Remote Sens.-basel.*, 13, 517,  
822 <https://doi.org/10.3390/rs13030517>, 2021.
- 823 Che, K., Liu, Y., Cai, Z., Yang, D., Wang, H., Ji, D., Yang, Y., and Wang, P.: Characterization of regional combustion efficiency  
824 using ΔXCO: ΔXCO<sub>2</sub> observed by a portable Fourier-Transform Spectrometer at an urban site in Beijing, *Adv. Atmos. Sci.*,  
825 39, 1299-1315, <https://doi.org/10.1007/s00376-022-1247-7>, 2022a.
- 826 Che, K., Cai, Z., Liu, Y., Wu, L., Yang, D., Chen, Y., Meng, X., Zhou, M., Wang, J., Yao, L., and Wang, P.: Lagrangian inversion  
827 of anthropogenic CO<sub>2</sub> emissions from Beijing using differential column measurements, *Environ. Res. Lett.*, 17,

828 <https://doi.org/10.1088/1748-9326/ac7477>, 2022b.

829 Chen, Y., Ma, Q., Lin, W., Xu, X., Yao, J., and Gao, W.: Measurement report: Long-term variations in carbon monoxide at a  
830 background station in China's Yangtze River Delta region, *Atmos. Chem. Phys.*, 20, 15969-15982,  
831 <https://doi.org/10.5194/acp-20-15969-2020>, 2020.

832 Chen, Y., Lu, Y., Qi, B., Ma, Q., Zang, K., Lin, Y., Liu, S., Pan, F., Li, S., and Guo, P.: Atmospheric CO<sub>2</sub> in the megacity  
833 Hangzhou, China: Urban-suburban differences, sources and impact factors, *Sci. Total Environ.*, 926, 171635,  
834 <https://doi.org/10.1016/j.scitotenv.2024.171635>, 2024.

835 Corro, L. M., Bagstad, K. J., Heris, M. P., Ibsen, P. C., Schleeuwis, K. G., Diffendorfer, J. E., Troy, A., Megown, K., and  
836 O'Neil-Dunne, J. P. M.: An enhanced national-scale urban tree canopy cover dataset for the United States, *Sci Data*, 12, 490,  
837 <https://doi.org/10.1038/s41597-025-04816-0>, 2025.

838 Crippa, M., Solazzo, E., Huang, G., Guizzardi, D., Koffi, E., Muntean, M., Schieberle, C., Friedrich, R., and Janssens-  
839 Maenhout, G.: High resolution temporal profiles in the Emissions Database for Global Atmospheric Research, *Scientific*  
840 *Data*, 7, <https://doi.org/10.1038/s41597-020-0462-2>, 2020.

841 Crippa, M., Guizzardi, D., Pisoni, E., Solazzo, E., Guion, A., Muntean, M., Florczyk, A., Schiavina, M., Melchiorri, M., and  
842 Hutfilter, A. F.: Global anthropogenic emissions in urban areas: patterns, trends, and challenges, *Environ. Res. Lett.*, 16,  
843 <https://doi.org/10.1088/1748-9326/ac00e2>, 2021.

844 Crippa, M., Guizzardi, D., Pagani, F., Banja, M., Muntean, M., Schaaf, E., Monforti-Ferrario, F., Becker, W. E., Quadrelli, R.,  
845 Riquez Martin, A., Taghavi-Moharamli, P., Köykkä, J., Grassi, G., Rossi, S., Melo, J., Oom, D., Branco, A., San-Miguel,  
846 J., Manca, G., Pisoni, E., Vignati, E., and Pekar, F.: GHG emissions of all world countries, Publications Office of the  
847 European Union, <https://doi.org/10.2760/4002897>, 2024.

848 Deng, A., Lauvaux, T., Davis, K. J., Gaudet, B. J., Miles, N., Richardson, S. J., Wu, K., Sarmiento, D. P., Hardesty, R. M., and  
849 Bonin, T. A.: Toward reduced transport errors in a high resolution urban CO<sub>2</sub> inversion system, *Elem Sci Anth*, 5, 20,  
850 <https://doi.org/10.1525/elementa.133>, 2017.

851 Didan, K.: MOD13A3 MODIS/Terra Vegetation Indices Monthly L3 Global 1km SIN Grid V006, NASA Land Processes  
852 Distributed Active Archive Center [dataset], <https://doi.org/10.5067/MODIS/MOD13A3.006>, 2015.

853 Dusenge, M. E., Duarte, A. G., and Way, D. A.: Plant carbon metabolism and climate change: elevated CO<sub>2</sub> and temperature  
854 impacts on photosynthesis, photorespiration and respiration, *New Phytol.*, 221, 32-49, <https://doi.org/10.1111/nph.15283>,  
855 2019.

856 Fasoli, B.: uataq/stilt: Geoscientific Model Development 2018 (v1.0), Zenodo [code], <https://doi.org/10.5281/zenodo.1196561>,  
857 2018.

858 Fasoli, B., Lin, J. C., Bowling, D. R., Mitchell, L., and Mendoza, D.: Simulating atmospheric tracer concentrations for spatially  
859 distributed receptors: updates to the Stochastic Time-Inverted Lagrangian Transport model's R interface (STILT-R version  
860 2), *Geosci. Model Dev.*, 11, 2813-2824, <https://doi.org/10.5194/gmd-11-2813-2018>, 2018.

861 Gao, S., Zhang, X., and Chen, M.: Spatiotemporal dynamics and driving forces of city-level CO<sub>2</sub> emissions in China from  
862 2000 to 2019, *J. Clean. Prod.*, 377, 134358, <https://doi.org/10.1016/j.jclepro.2022.134358>, 2022.

863 Gao, Y., Lee, X., Liu, S., Hu, N., Wei, X., Hu, C., Liu, C., Zhang, Z., and Yang, Y.: Spatiotemporal variability of the near-  
864 surface CO<sub>2</sub> concentration across an industrial-urban-rural transect, Nanjing, China, *Sci. Total Environ.*, 631, 1192-1200,  
865 <https://doi.org/10.1016/j.scitotenv.2018.03.126>, 2018.

866 Gately, C. K. and Hutyra, L. R.: Large Uncertainties in Urban - Scale Carbon Emissions, *J. Geophys. Res.-Atmos.*, 122,  
867 <https://doi.org/10.1002/2017jd027359>, 2017.

868 George, K., Ziska, L. H., Bunce, J. A., and Quebedeaux, B.: Elevated atmospheric CO<sub>2</sub> concentration and temperature across  
869 an urban-rural transect, *Atmos. Environ.*, 41, 7654-7665, <https://doi.org/10.1016/j.atmosenv.2007.08.018>, 2007.

870 Gerbig, C., Lin, J., Wofsy, S., Daube, B., Andrews, A., Stephens, B., Bakwin, P., and Grainger, C.: Toward constraining  
871 regional - scale fluxes of CO<sub>2</sub> with atmospheric observations over a continent: 2. Analysis of COBRA data using a  
872 receptor - oriented framework, *J. Geophys. Res.-Atmos.*, 108, <https://doi.org/10.1029/2002JD003018>, 2003.

873 Glauch, T., Marshall, J., Gerbig, C., Botía, S., Galkowski, M., Vardag, S. N., and Butz, A.: pyVPRM: A next-generation

874 Vegetation Photosynthesis and Respiration Model for the post-MODIS era, *Geosci. Model Dev.*, 18, 4713-4742,  
875 <https://doi.org/10.5194/gmd-18-4713-2025>, 2025.

876 Griffin, R. J., Chen, J., Carmody, K., Vutukuru, S., and Dabdub, D.: Contribution of gas phase oxidation of volatile organic  
877 compounds to atmospheric carbon monoxide levels in two areas of the United States, *J. Geophys. Res.-Atmos.*, 112,  
878 <https://doi.org/10.1029/2006JD007602>, 2007.

879 Guangzhou Municipal Bureau of Statistics: Guangzhou Statistical Yearbook 2024, Tech. rep.,  
880 [https://tjj.gz.gov.cn/datav/admin/home/www\\_nj/](https://tjj.gz.gov.cn/datav/admin/home/www_nj/) (last access: 1 December 2025), 2024.

881 Gurney, K. R., Patarasuk, R., Liang, J., Song, Y., O'Keeffe, D., Rao, P., Whetstone, J. R., Duren, R. M., Eldering, A., and Miller,  
882 C.: The Hestia fossil fuel CO<sub>2</sub> emissions data product for the Los Angeles megacity (Hestia-LA), *Earth Syst. Sci. Data*, 11,  
883 1309-1335, <https://doi.org/10.5194/essd-11-1309-2019>, 2019.

884 Han, P., Yao, B., Cai, Q., Chen, H., Sun, W., Liang, M., Zhang, X., Zhao, M., Martin, C., Liu, Z., Ye, H., Wang, P., Li, Y., and  
885 Zeng, N.: Support Carbon Neutral Goal with a High-Resolution Carbon Monitoring System in Beijing, *B. Am. Meteorol.*  
886 *Soc.*, 105, E2461-E2481, <https://doi.org/10.1175/bams-d-23-0025.1>, 2024.

887 Han, S., Kondo, Y., Oshima, N., Takegawa, N., Miyazaki, Y., Hu, M., Lin, P., Deng, Z., Zhao, Y., and Sugimoto, N.: Temporal  
888 variations of elemental carbon in Beijing, *J. Geophys. Res.-Atmos.*, 114, <https://doi.org/10.1029/2009JD012027>, 2009.

889 Hao, T., Chen, S., Liu, J., Tang, Y., and Han, S.: An observational study on the impact of sea-land breeze and low-level jet on  
890 air pollutant transport in the Bohai Bay, *Atmos. Pollut. Res.*, 15, 102143, <https://doi.org/10.1016/j.apr.2024.102143>, 2024.

891 Hao, T., Chen, S., Cai, Z., Shan, X., Meng, L., Han, S., and Dong, G.: Influence of sea breeze on atmospheric pollutant  
892 concentration over Tianjin, *China Environmental Science*, 37(9), 3247-3257, <https://doi.org/10.3969/j.issn.1000-6923.2017.09.006>, 2017.

894 He, H., Kramer, R. J., Soden, B. J., and Jeevanjee, N.: State dependence of CO<sub>2</sub> forcing and its implications for climate  
895 sensitivity, *Science*, 382, 7, <https://doi.org/10.1126/science.abq6872>, 2023.

896 Hersbach, H., Bell, B., Berrisford, P., Biavati, G., Horányi, A., Muñoz Sabater, J., Nicolas, J., Peubey, C., Radu, R., Rozum,  
897 I., Schepers, D., Simmons, A., Soci, C., Dee, D., Thépaut, J.-N.: ERA5 hourly data on single levels from 1940 to present,  
898 Copernicus Climate Change Service (C3S) Climate Data Store (CDS) [dataset], <https://doi.org/10.24381/cds.adbb2d47>,  
899 2023.

900 Hu, M., Wang, Y., Wang, S., Jiao, M., Huang, G., and Xia, B.: Spatial-temporal heterogeneity of air pollution and its  
901 relationship with meteorological factors in the Pearl River Delta, China, *Atmos. Environ.*, 254, 118415,  
902 <https://doi.org/10.1016/j.atmosenv.2021.118415>, 2021.

903 Huang, Y., Li, S., Zhu, Y., Liu, Y., Hong, Y., Chen, X., Deng, W., Xi, X., Lu, X., and Fan, Q.: Increasing sea - land breeze  
904 frequencies over coastal areas of China in the past five decades, *Geophys. Res. Lett.*, 52, e2024GL112480,  
905 <https://doi.org/10.1029/2024GL112480>, 2025.

906 Hüser, I., Harder, H., Heil, A., and Kaiser, J. W.: Assumptions about footprint layer heights influence the quantification of  
907 emission sources: a case study for Cyprus, *Atmos. Chem. Phys.*, 17, 10955-10967, <https://doi.org/10.5194/acp-17-10955-2017>, 2017.

909 Jacobson, A. R., Schuldt, K. N., Andrews, A., Miller, J. B., Oda, T., Basu, S., Mund, J., Weir, B., Ott, L., Aalto, T., Abshire, J.  
910 B., Aikin, K., Allen, G., Andrade, M., Apadula, F., Arnold, S., Baier, B., Bakwin, P., Bartyzel, J., Bentz, G., Bergamaschi,  
911 P., Beyersdorf, A., Biermann, T., Biraud, S. C., Blanc, P.-E., Boenisch, H., Bowling, D., Brailsford, G., Brand, W. A.,  
912 Brunner, D., Bui, T. P., Burban, B., Băni, L., Calzolari, F., Chang, C. S., Chen, H., Chen, G., Chmura, L., Clark, S., Climadat,  
913 S., Colomb, A., Commane, R., Condori, L., Conen, F., Conil, S., Couret, C., Cristofanelli, P., Cuevas, E., Curcoll, R., Daube,  
914 B., Davis, K. J., De Mazière, M., De Wekker, S., Dean-Day, J. M., Della Coletta, J., Delmotte, M., Di Iorio, T., DiGangi,  
915 E., DiGangi, J. P., Dickerson, R., Elsasser, M., Emmenegger, L., Fang, S., Forster, G., France, J., Frumau, A., Fuente-Lastra,  
916 M., Galkowski, M., Gatti, L. V., Gehrlein, T., Gerbig, C., Gheusi, F., Gloor, E., Goto, D., Griffis, T., Hammer, S., Hanisco,  
917 T. F., Hanson, C., Haszpra, L., Hatakka, J., Heimann, M., Heliasz, M., Heltai, D., Henne, S., Hensen, A., Hermans, C.,  
918 Hermansen, O., Hintsa, E., Hoheisel, A., Holst, J., Iraci, L. T., Ivakhov, V., Jaffe, D. A., Jordan, A., Joubert, W., Kang, H.-  
919 Y., Karion, A., Kawa, S. R., Kazan, V., Keeling, R. F., Keronen, P., Kim, J., Klausen, J., Kneuer, T., Ko, M.-Y., Kolari, P.,

920 Kominkova, K., Kort, E., Kozlova, E., Krummel, P. B., Kubistin, D., Kulawik, S. S., Kumps, N., Labuschagne, C., Lam, D.  
921 H., Lan, X., Langenfelds, R. L., Lanza, A., Laurent, O., Laurila, T., Lauvaux, T., Lavric, J., Law, B. E., Lee, C.-H., Lee, J.,  
922 Lehner, I., Lehtinen, K., Leppert, R., Leskinen, A., Leuenberger, M., Leung, W. H., Levin, I., Levula, J., Lin, J., Lindauer,  
923 M., Lindroth, A., Loh, Z. M., Lopez, M., Lunder, C. R., Löfvenius, M. O., Machida, T., Mammarella, I., Manca, G., Manning,  
924 A., Manning, A., Marek, M. V., Marklund, P., Marrero, J. E., Martin, M. Y., Martin, D., Martins, G. A., Matsueda, H.,  
925 McKain, K., Meijer, H., Meinhardt, F., Merchant, L., Metzger, J.-M., Mihalopoulos, N., Miles, N. L., Miller, C. E., Mitchell,  
926 L., Monteiro, V., Montzka, S., Moossen, H., Moreno, C., Morgan, E., Morgui, J.-A., Morimoto, S., Munger, J. W., Munro,  
927 D., Mutuku, M., Myhre, C. L., Mölder, M., Müller-Williams, J., Nakaoka, S.-I., Necki, J., Newman, S., Nichol, S., Nisbet,  
928 E., Niwa, Y., Njiru, D. M., Noe, S. M., Nojiri, Y., O'Doherty, S., Obersteiner, F., Paplawsky, B., Parworth, C. L., Peischl, J.,  
929 Peltola, O., Peters, W., Philippon, C., Piacentino, S., Pichon, J. M., Pickers, P., Piper, S., Pitt, J., Plass-Dülmer, C., Platt, S.  
930 M., Prinzivalli, S., Ramonet, M., Ramos, R., Ren, X., Reyes-Sanchez, E., Richardson, S. J., Rigouleau, L.-J., Riris, H.,  
931 Rivas, P. P., Rothe, M., Roulet, Y.-A., Ryerson, T., Ryoo, J.-M., Sargent, M., Sasakawa, M., Schaefer, H., Scheeren, B.,  
932 Schmidt, M., Schuck, T., Schumacher, M., Seibel, J., Seifert, T., Sha, M. K., Shepson, P., Shin, D., Shook, M., Sloop, C. D.,  
933 Smale, D., Smith, P. D., Spain, G., St. Clair, J. M., Steger, D., Steinbacher, M., Stephens, B., Sweeney, C., Sørensen, L. L.,  
934 Taipale, R., Takatsuji, S., Tans, P., Thoning, K., Timas, H., Torn, M., Trisolino, P., Turnbull, J., Vermeulen, A., Viner, B.,  
935 Vitkova, G., Walker, S., Watson, A., Weiss, R., Weyrauch, D., Wofsy, S. C., Worsley, J., Worthy, D., Xueref-Remy, I., Yates,  
936 E. L., Young, D., Yver-Kwok, C., Zaehle, S., Zahn, A., Zellweger, C., Zimnoch, M., de Souza, R. A., di Sarra, A. G., van  
937 Dinter, D., and van den Bulk, P.: CarbonTracker CT-NRT.v2024-5, NOAA Earth System Research Laboratory [dataset],  
938 <https://doi.org/10.15138/atpd-k925>, 2024.

939 Kim, J., Berelson, W. M., Rollins, N. E., Asimow, N. G., Newman, C., Cohen, R. C., Miller, J. B., McDonald, B. C., Peischl,  
940 J., and Lehman, S. J.: Observing Anthropogenic and Biogenic CO<sub>2</sub> Emissions in Los Angeles Using a Dense Sensor  
941 Network, *Environ Sci Technol*, 59, 3508-3517, <https://doi.org/10.1021/acs.est.4c11392>, 2025.

942 Kumar, P.: Climate change and cities: challenges ahead, *Front. Sustain. Cities*, 3, 645613,  
943 <https://doi.org/10.3389/frsc.2021.645613>, 2021.

944 Kunik, L., Mallia, D. V., Gurney, K. R., Mendoza, D. L., Oda, T., and Lin, J. C.: Bayesian inverse estimation of urban CO<sub>2</sub>  
945 emissions: Results from a synthetic data simulation over Salt Lake City, UT, *Elem Sci Anth*, 7, 36,  
946 <https://doi.org/10.1525/elementa.375>, 2019.

947 Lauvaux, T., Miles, N. L., Deng, A., Richardson, S. J., Cambaliza, M. O., Davis, K. J., Gaudet, B., Gurney, K. R., Huang, J.,  
948 O'Keefe, D., Song, Y., Karion, A., Oda, T., Patarasuk, R., Razlivanov, I., Sarmiento, D., Shepson, P., Sweeney, C., Turnbull,  
949 J., and Wu, K.: High-resolution atmospheric inversion of urban CO<sub>2</sub> emissions during the dormant season of the Indianapolis  
950 Flux Experiment (INFLUX), *J. Geophys. Res.-Atmos.*, 121, 5213-5236, <https://doi.org/10.1002/2015JD024473>, 2016.

951 Lei, B.-Q., Li, L., and Chan, P. W.: Long-term trend in the sea-land breeze in Hong Kong, *Urban. Clim.*, 55, 101981,  
952 <https://doi.org/10.1016/j.uclim.2024.101981>, 2024.

953 Leroyer, S., Bélair, S., Husain, S. Z., and Mailhot, J.: Subkilometer numerical weather prediction in an urban coastal area: A  
954 case study over the Vancouver metropolitan area, *J. Appl. Meteorol. Clim.*, 53, 1433-1453, [https://doi.org/10.1175/JAMC-](https://doi.org/10.1175/JAMC-D-13-0202.1)  
955 [D-13-0202.1](https://doi.org/10.1175/JAMC-D-13-0202.1), 2014.

956 Lian, J., Lauvaux, T., Utard, H., Bréon, F.-M., Broquet, G., Ramonet, M., Laurent, O., Albarus, I., Chariot, M., and Kotthaus,  
957 S.: Can we use atmospheric CO<sub>2</sub> measurements to verify emission trends reported by cities? Lessons from a 6-year  
958 atmospheric inversion over Paris, *Atmos. Chem. Phys.*, 23, 8823-8835, <https://doi.org/10.5194/acp-23-8823-2023>, 2023.

959 Lin, J. C., Bares, R., Fasoli, B., Garcia, M., Crosman, E., and Lyman, S.: Declining methane emissions and steady, high leakage  
960 rates observed over multiple years in a western US oil/gas production basin, *Sci. Rep-uk.*, 11, 22291,  
961 <https://doi.org/10.1038/s41598-021-01721-5>, 2021.

962 Lin, J. C., Gerbig, C., Wofsy, S., Andrews, A., Daube, B., Davis, K., and Grainger, C.: A near - field tool for simulating the  
963 upstream influence of atmospheric observations: The Stochastic Time - Inverted Lagrangian Transport (STILT) model, *J.*  
964 *Geophys. Res.-Atmos.*, 108(D16), <https://doi.org/10.1029/2002JD003161>, 2003.

965 Liu, C., Huang, J.-P., Diao, Y.-W., Wen, X.-F., Xiao, W., Zhang, M., Lee, X.-H., and Liu, S.-D.: Optimization and evaluation

966 of vegetation photosynthesis and respiration model using the measurements collected from the forest site of subtropical  
967 coniferous-evergreen, *Chinese Journal of Plant Ecology*, 39, 388-397, <https://doi.org/10.17521/cjpe.2015.0038>, 2015.

968 Liu, H., Chan, J. C., and Cheng, A. Y.: Internal boundary layer structure under sea-breeze conditions in Hong Kong, *Atmos.*  
969 *Environ.*, 35, 683-692, [https://doi.org/10.1016/S1352-2310\(00\)00335-6](https://doi.org/10.1016/S1352-2310(00)00335-6), 2001.

970 Liu, W., Niu, Z., Feng, X., Zhou, W., Liang, D., Wang, G., and Liu, L.: Determining the key meteorological factors affecting  
971 atmospheric CO<sub>2</sub> and CH<sub>4</sub> using machine learning algorithms at a suburban site in China, *Urban. Clim.*, 59, 102312,  
972 <https://doi.org/10.1016/j.uclim.2025.102312>, 2025.

973 Ma, M., Gao, Y., Ding, A., Su, H., Liao, H., Wang, S., Wang, X., Zhao, B., Zhang, S., Fu, P., Guenther, A. B., Wang, M., Li,  
974 S., Chu, B., Yao, X., and Gao, H.: Development and Assessment of a High-Resolution Biogenic Emission Inventory from  
975 Urban Green Spaces in China, *Environ Sci Technol*, 56, 175-184, <https://doi.org/10.1021/acs.est.1c06170>, 2022.

976 Mai, B., Deng, X., Liu, X., Li, T., Guo, J., and Ma, Q.: The climatology of ambient CO<sub>2</sub> concentrations from long-term  
977 observation in the Pearl River Delta region of China: Roles of anthropogenic and biogenic processes, *Atmos. Environ.*, 251,  
978 118266, <https://doi.org/10.1016/j.atmosenv.2021.118266>, 2021.

979 Mai, B., Diao, Y., Yang, H., Deng, T., Zou, Y., Wang, Y., Lan, W., Liu, X., and Deng, X.: Assessing atmospheric CO<sub>2</sub>  
980 concentrations and contributions from biogenic and anthropogenic sources in the Pearl River Delta region, *Urban. Clim.*,  
981 54, 101864, <https://doi.org/10.1016/j.uclim.2024.101864>, 2024a.

982 Mai, J., Yu, L., Deng, T., Wu, D., Qing, P., and Yu, X.: Impact of sea-land breezes on the ozone pollution over the Pearl River  
983 Estuary, *China Environmental Science*, 45(03), 1198-1209, <https://doi.org/10.19674/j.cnki.issn1000-6923.20241102.001>,  
984 2024b.

985 Menzer, O. and McFadden, J. P.: Statistical partitioning of a three-year time series of direct urban net CO<sub>2</sub> flux measurements  
986 into biogenic and anthropogenic components, *Atmos. Environ.*, 170, 319-333,  
987 <https://doi.org/10.1016/j.atmosenv.2017.09.049>, 2017.

988 Miller, J. B., Lehman, S. J., Verhulst, K. R., Miller, C. E., Duren, R. M., Yadav, V., Newman, S., and Sloop, C. D.: Large and  
989 seasonally varying biospheric CO<sub>2</sub> fluxes in the Los Angeles megacity revealed by atmospheric radiocarbon, *P. Natl. Acad.*  
990 *Sci. Usa.*, 117, 26681-26687, <https://doi.org/10.1073/pnas.2005253117>, 2020.

991 Mitchell, L. E., Lin, J. C., Bowling, D. R., Pataki, D. E., Strong, C., Schauer, A. J., Bares, R., Bush, S. E., Stephens, B. B., and  
992 Mendoza, D.: Long-term urban carbon dioxide observations reveal spatial and temporal dynamics related to urban  
993 characteristics and growth, *P. Natl. Acad. Sci. Usa.*, 115, 2912-2917, <https://doi.org/10.1073/pnas.1702393115>, 2018.

994 Nalini, K., Lauvaux, T., Abdallah, C., Lian, J., Ciais, P., Utard, H., Laurent, O., and Ramonet, M.: High - resolution Lagrangian  
995 inverse modeling of CO<sub>2</sub> emissions over the Paris region during the first 2020 lockdown period, *J. Geophys. Res.-Atmos.*,  
996 127, e2021JD036032, <https://doi.org/10.1029/2021JD036032>, 2022.

997 Newman, S., Jeong, S., Fischer, M., Xu, X., Haman, C., Lefer, B., Alvarez, S., Rappenglueck, B., Kort, E., and Andrews, A.:  
998 Diurnal tracking of anthropogenic CO<sub>2</sub> emissions in the Los Angeles basin megacity during spring 2010, *Atmos. Chem.*  
999 *Phys.*, 13, 4359-4372, <https://doi.org/10.5194/acp-13-4359-2013>, 2013.

1000 Pan, C., Zhu, X., Wei, N., Zhu, X., She, Q., Jia, W., Liu, M., and Xiang, W.: Spatial variability of daytime CO<sub>2</sub> concentration  
1001 with landscape structure across urbanization gradients, Shanghai, China, *Clim. Res.*, 69, 107-116,  
1002 <https://doi.org/10.3354/cr01394>, 2016.

1003 Park, C., Jeong, S., Shin, Y.-s., Cha, Y.-s., and Lee, H.-c.: Reduction in urban atmospheric CO<sub>2</sub> enhancement in Seoul, South  
1004 Korea, resulting from social distancing policies during the COVID-19 pandemic, *Atmos. Pollut. Res.*, 12, 101176,  
1005 <https://doi.org/10.1016/j.apr.2021.101176>, 2021.

1006 Pitt, J. R., Lopez-Coto, I., Hajny, K. D., Tomlin, J., Kaeser, R., Jayarathne, T., Stirm, B. H., Floerchinger, C. R., Loughner, C.  
1007 P., and Gately, C. K.: New York City greenhouse gas emissions estimated with inverse modeling of aircraft measurements,  
1008 *Elem Sci Anth*, 10, 00082, <https://doi.org/10.1525/elementa.2021.00082>, 2022.

1009 Qingdao Municipal Bureau of Statistics: Qingdao Statistical Yearbook 2024, Tech. rep.,  
1010 [http://qdtj.qingdao.gov.cn/tongjisi/tjsj\\_tjni/tjni\\_2024/202501/P020250114376271252952.pdf](http://qdtj.qingdao.gov.cn/tongjisi/tjsj_tjni/tjni_2024/202501/P020250114376271252952.pdf) (last access: 1 December  
1011 2025), 2024.

- 1012 Qiu, X. and Fan, S.: Study on the application of auto-meteorological station data in local circulations analysis such as the sea-  
 1013 land breeze, *Acta Scientiarum Naturalium Universitatis Sunyatseni*, 52(2), 133-136,  
 1014 <https://doi.org/10.13471/j.cnki.acta.snus.2013.02.025>, 2013.
- 1015 Reddy, T. R., Mehta, S. K., Ananthavel, A., Ali, S., Annamalai, V., and Rao, D. N.: Seasonal characteristics of sea breeze and  
 1016 thermal internal boundary layer over Indian east coast region, *Meteorol. Atmos. Phys.*, 133, 217-232,  
 1017 <https://doi.org/10.1007/s00703-020-00746-1>, 2021.
- 1018 Sargent, M., Barrera, Y., Nehrkorn, T., Hutyra, L. R., Gately, C. K., Jones, T., McKain, K., Sweeney, C., Hegarty, J., Hardiman,  
 1019 B., Wang, J. A., and Wofsy, S. C.: Anthropogenic and biogenic CO<sub>2</sub> fluxes in the Boston urban region, *P. Natl. Acad. Sci.*  
 1020 *Usa.*, 115, 7491-7496, <https://doi.org/10.1073/pnas.1803715115>, 2018.
- 1021 Schuldt, K. N., Mund, J., Aalto, T., Abshire, J. B., Aikin, K., Allen, G., Andrade, M., Andrews, A., Apadula, F., Arnold, S.,  
 1022 Baier, B., Bakwin, P., Bartyzel, J., Bentz, G., Bergamaschi, P., Beyersdorf, A., Biermann, T., Biraud, S. C., Blanc, P.-E.,  
 1023 Boenisch, H., Bowling, D., Brailsford, G., Brand, W. A., Brunner, D., Bui, T. P., Burban, B., Bani, L., Calzolari, F., Chang,  
 1024 C. S., Chen, H., Chen, G., Chmura, L., Clark, S., Climadat, S., Colomb, A., Commane, R., Condori, L., Conen, F., Conil,  
 1025 S., Couret, C., Cristofanelli, P., Cuevas, E., Curcoll, R., Daube, B., Davis, K. J., De Mazière, M., De Wekker, S., Dean-Day,  
 1026 J. M., Della Coletta, J., Delmotte, M., Di Iorio, T., DiGangi, E., DiGangi, J. P., Dickerson, R., Elsasser, M., Emmenegger,  
 1027 L., Fang, S., Forster, G., France, J., Frumau, A., Fuente-Lastra, M., Galkowski, M., Gatti, L. V., Gehrlein, T., Gerbig, C.,  
 1028 Gheusi, F., Gloor, E., Goto, D., Griffis, T., Hammer, S., Hanisco, T. F., Hanson, C., Haszpra, L., Hatakka, J., Heimann, M.,  
 1029 Heliasz, M., Heltai, D., Henne, S., Hensen, A., Hermans, C., Hermansen, O., Hintsä, E., Hoheisel, A., Holst, J., Iraci, L. T.,  
 1030 Ivakhov, V., Jaffé, D. A., Jordan, A., Joubert, W., Kang, H.-Y., Karion, A., Kawa, S. R., Kazan, V., Keeling, R. F., Keronen,  
 1031 P., Kim, J., Klausen, J., Kneuer, T., Ko, M.-Y., Kolari, P., Kominkova, K., Kort, E., Kozlova, E., Krummel, P. B., Kubistin,  
 1032 D., Kulawik, S. S., Kumps, N., Labuschagne, C., Lam, D. H., Lan, X., Langenfelds, R. L., Lanza, A., Laurent, O., Laurila,  
 1033 T., Lauvaux, T., Lavric, J., Law, B. E., Lee, C.-H., Lee, J., Lehner, I., Lehtinen, K., Leppert, R., Leskinen, A., Leuenberger,  
 1034 M., Leung, W. H., Levin, I., Levula, J., Lin, J., Lindauer, M., Lindroth, A., Loh, Z. M., Lopez, M., Lunder, C. R., Löfvenius,  
 1035 M. O., Machida, T., Mammarella, I., Manca, G., Manning, A., Manning, A., Marek, M. V., Marklund, P., Marrero, J. E.,  
 1036 Martin, M. Y., Martin, D., Martins, G. A., Matsueda, H., McKain, K., Meijer, H., Meinhardt, F., Merchant, L., Metzger, J.-  
 1037 M., Mihalopoulos, N., Miles, N. L., Miller, C. E., Miller, J. B., Mitchell, L., Monteiro, V., Montzka, S., Moossen, H.,  
 1038 Moreno, C., Morgan, E., Morgui, J.-A., Morimoto, S., Munger, J. W., Munro, D., Mutuku, M., Myhre, C. L., Mölder, M.,  
 1039 Müller-Williams, J., Nakaoka, S.-I., Necki, J., Newman, S., Nichol, S., Nisbet, E., Niwa, Y., Njiru, D. M., Noe, S. M., Nojiri,  
 1040 Y., O'Doherty, S., Obersteiner, F., Paplawsky, B., Parworth, C. L., Peischl, J., Peltola, O., Peters, W., Philippon, C.,  
 1041 Piacentino, S., Pichon, J. M., Pickers, P., Piper, S., Pitt, J., Plass-Dülmer, C., Platt, S. M., Prinzivalli, S., Ramonet, M.,  
 1042 Ramos, R., Ren, X., Reyes-Sanchez, E., Richardson, S. J., Rigoulet, L.-J., Riris, H., Rivas, P. P., Rothe, M., Roulet, Y.-A.,  
 1043 Ryerson, T., Ryoo, J.-M., Sargent, M., Sasakawa, M., Schaefer, H., Scheeren, B., Schmidt, M., Schuck, T., Schumacher, M.,  
 1044 Seibel, J., Seifert, T., Sha, M. K., Shepson, P., Shin, D., Shook, M., Sloop, C. D., Smale, D., Smith, P. D., Spain, G., St.  
 1045 Clair, J. M., Steger, D., Steinbacher, M., Stephens, B., Sweeney, C., Sørensen, L. L., Taipale, R., Takatsuji, S., Tans, P.,  
 1046 Thoning, K., Timas, H., Torn, M., Trisolino, P., Turnbull, J., Vermeulen, A., Viner, B., Vitkova, G., Walker, S., Watson, A.,  
 1047 Weiss, R., Weyrauch, D., Wofsy, S. C., Worsey, J., Worthy, D., Xueref-Remy, I., Yates, E. L., Young, D., Yver-Kwok, C.,  
 1048 Zaehle, S., Zahn, A., Zellweger, C., Zimnoch, M., de Souza, R. A., di Sarra, A. G., van Dinter, D., and van den Bulk, P.:  
 1049 Multi-laboratory compilation of atmospheric carbon dioxide data for the period 1957-2023  
 1050 (obspack\_co2\_1\_test\_GLOBALVIEWplus\_v10.1\_2024-11-13), NOAA Earth System Research Laboratory, Global  
 1051 Monitoring Laboratory [dataset], <https://doi.org/10.25925/20241101>, 2024.
- 1052 Shen, L., Zhao, C., and Yang, X.: Climate - driven characteristics of sea - land breezes over the globe, *Geophys. Res. Lett.*,  
 1053 48, e2020GL092308, <https://doi.org/10.1029/2020GL092308>, 2021.
- 1054 Shen, L., Zhao, C., Ma, Z., Li, Z., Li, J., and Wang, K.: Observed decrease of summer sea-land breeze in Shanghai from 1994  
 1055 to 2014 and its association with urbanization, *Atmos. Res.*, 227, 198-209, <https://doi.org/10.1016/j.atmosres.2019.05.007>,  
 1056 2019.
- 1057 Shen, L., Zhao, C., Xu, C., Yan, Y., Chen, A., Yang, Y., Hang, R., Zhu, Y., Zhang, Z., and Song, X.: Effects of sea land breeze

1058 on air - sea turbulent heat fluxes in different seasons using platform observation in East China Sea, *J. Geophys. Res.-Atmos.*,  
1059 129, e2023JD040001, <https://doi.org/10.1029/2023JD040001>, 2024.

1060 Shenzhen Municipal Bureau of Statistics: Shenzhen Statistical Yearbook, Tech. rep.,  
1061 <https://tjj.sz.gov.cn/attachment/1/1568/1568796/12061198.pdf> (last access: 1 December 2025), 2024.

1062 Shusterman, A. A., Kim, J., Lieschke, K. J., Newman, C., Wooldridge, P. J., and Cohen, R. C.: Observing local CO<sub>2</sub> sources  
1063 using low-cost, near-surface urban monitors, *Atmos. Chem. Phys.*, 18, 13773-13785, [https://doi.org/10.5194/acp-18-13773-](https://doi.org/10.5194/acp-18-13773-2018)  
1064 [2018](https://doi.org/10.5194/acp-18-13773-2018), 2018.

1065 Soininen, J., Kohonen, K.-M., Rantala, P., Kulmala, L., Aaltonen, H., and Järvi, L.: Carbon uptake of an urban green space  
1066 inferred from carbonyl sulfide fluxes, *npj Clim Atmos Sci*, 8, <https://doi.org/10.1038/s41612-025-00958-5>, 2025.

1067 Stauffer, R. M., Thompson, A. M., Martins, D. K., Clark, R. D., Goldberg, D. L., Loughner, C. P., Delgado, R., Dickerson, R.  
1068 R., Stehr, J. W., and Tzortziou, M. A.: Bay breeze influence on surface ozone at Edgewood, MD during July 2011, *J. Atmos.*  
1069 *Chem.*, 72, 335-353, <https://doi.org/10.1007/s10874-012-9241-6>, 2015.

1070 Sun, L., Tian, W., Zhang, W., Liu, C., and Fang, C.: Characteristics of sea-land breezes and their impact on PM<sub>2.5</sub> and O<sub>3</sub> in  
1071 Shanghai and adjacent areas, *Acta Scientiae Circumstantiae*, 42(9), 339-350, <https://doi.org/10.13671/j.hjkkxb.2022.0111>,  
1072 2022.

1073 Tianjin Municipal Bureau of Statistics: Tianjin Statistical Yearbook, Tech. rep.,  
1074 <https://stats.tj.gov.cn/nianjian/2024nj/zk/indexch.htm> (last access: 1 December 2025), 2024.

1075 Turnbull, J. C., Karion, A., Davis, K. J., Lauvaux, T., Miles, N. L., Richardson, S. J., Sweeney, C., McKain, K., Lehman, S. J.,  
1076 and Gurney, K. R.: Synthesis of urban CO<sub>2</sub> emission estimates from multiple methods from the Indianapolis Flux Project  
1077 (INFLUX), *Environ. Sci. Technol.*, 53, 287-295, <https://doi.org/10.1021/acs.est.8b05552>, 2018.

1078 Turnbull, J. C., Sweeney, C., Karion, A., Newberger, T., Lehman, S. J., Tans, P. P., Davis, K. J., Lauvaux, T., Miles, N. L., and  
1079 Richardson, S. J.: Toward quantification and source sector identification of fossil fuel CO<sub>2</sub> emissions from an urban area:  
1080 Results from the INFLUX experiment, *J. Geophys. Res.-Atmos.*, 120, 292-312, <https://doi.org/10.1002/2014JD022555>,  
1081 2015.

1082 Turnbull, J. C., Tans, P. P., Lehman, S. J., Baker, D., Conway, T. J., Chung, Y., Gregg, J., Miller, J. B., Southon, J. R., and Zhou,  
1083 L. X.: Atmospheric observations of carbon monoxide and fossil fuel CO<sub>2</sub> emissions from East Asia, *J. Geophys. Res.-*  
1084 *Atmos.*, 116, <https://doi.org/10.1029/2011JD016691>, 2011.

1085 Velasco, E., Roth, M., Tan, S., Quak, M., Nabarro, S., and Norford, L.: The role of vegetation in the CO<sub>2</sub> flux from a tropical  
1086 urban neighbourhood, *Atmos. Chem. Phys.*, 13, 10185-10202, <https://doi.org/10.5194/acp-13-10185-2013>, 2013.

1087 Verhulst, K. R., Karion, A., Kim, J., Salameh, P. K., Keeling, R. F., Newman, S., Miller, J., Sloop, C., Pongetti, T., and Rao,  
1088 P.: Carbon dioxide and methane measurements from the Los Angeles Megacity Carbon Project—Part 1: calibration, urban  
1089 enhancements, and uncertainty estimates, *Atmos. Chem. Phys.*, 17, 8313-8341, <https://doi.org/10.5194/acp-17-8313-2017>,  
1090 2017.

1091 Vimont, I. J., Turnbull, J. C., Petrenko, V. V., Place, P. F., Sweeney, C., Miles, N., Richardson, S., Vaughn, B. H., and White,  
1092 J. W.: An improved estimate for the  $\delta^{13}\text{C}$  and  $\delta^{18}\text{O}$  signatures of carbon monoxide produced from atmospheric oxidation of  
1093 volatile organic compounds, *Atmos. Chem. Phys.*, 19, 8547-8562, <https://doi.org/10.5194/acp-19-8547-2019>, 2019.

1094 Wang, B., Geddes, J. A., Adams, T. J., Lind, E. S., McDonald, B. C., He, J., Harkins, C., Li, D., and Pfister, G. G.: Implications  
1095 of sea breezes on air quality monitoring in a coastal urban environment: Evidence from high resolution modeling of NO<sub>2</sub>  
1096 and O<sub>3</sub>, *J. Geophys. Res.-Atmos.*, 128, e2022JD037860, <https://doi.org/10.1029/2022JD037860>, 2023.

1097 Wang, P., Zhou, W., Niu, Z., Xiong, X., Wu, S., Cheng, P., Hou, Y., Lu, X., and Du, H.: Spatio-temporal variability of  
1098 atmospheric CO<sub>2</sub> and its main causes: A case study in Xi'an city, China, *Atmos. Res.*, 249, 105346,  
1099 <https://doi.org/10.1016/j.atmosres.2020.105346>, 2021.

1100 Wang, P., Zhou, W., Xiong, X., Wu, S., Niu, Z., Yu, Y., Liu, J., Feng, T., Cheng, P., and Du, H.: Source attribution of atmospheric  
1101 CO<sub>2</sub> using <sup>14</sup>C and <sup>13</sup>C as tracers in two Chinese megacities during winter, *J. Geophys. Res.-Atmos.*, 127, e2022JD036504,  
1102 <https://doi.org/10.1029/2022JD036504>, 2022.

1103 Wang, Y., Munger, J., Xu, S., McElroy, M. B., Hao, J., Nielsen, C., and Ma, H.: CO<sub>2</sub> and its correlation with CO at a rural site

1104 near Beijing: implications for combustion efficiency in China, *Atmos. Chem. Phys.*, 10, 8881-8897,  
1105 <https://doi.org/10.5194/acp-10-8881-2010>, 2010.

1106 Wei, D., Reinmann, A., Schiferl, L. D., and Commane, R.: High resolution modeling of vegetation reveals large summertime  
1107 biogenic CO<sub>2</sub> fluxes in New York City, *Environ. Res. Lett.*, 17, 124031, <https://doi.org/10.1088/1748-9326/aca68f>, 2022.

1108 WMO: WMO Greenhouse Gas Bulletin No. 20 – The State of Greenhouse Gases in the Atmosphere Based on Global  
1109 Observations through 2023, Tech. rep., <https://library.wmo.int/idurl/4/69057> (last access: 18 June 2025), 2024.

1110 WMO: GAW Report No. 314 – Integrated Global Greenhouse Gas Information System: Urban Emission Observation and  
1111 Monitoring Good Research Practice Guidelines, Tech. rep., <https://library.wmo.int/idurl/4/69623> (last access: 1 December  
1112 2025), 2025.

1113 Wu, D., Lin, J. C., Duarte, H. F., Yadav, V., Parazoo, N. C., Oda, T., and Kort, E. A.: A model for urban biogenic CO<sub>2</sub> fluxes:  
1114 Solar-Induced Fluorescence for Modeling Urban biogenic Fluxes (SMUrF v1), *Geosci. Model Dev.*, 14, 3633-3661,  
1115 <https://doi.org/10.5194/gmd-14-3633-2021>, 2021.

1116 Wu, D., Liu, J., Wennberg, P. O., Palmer, P. I., Nelson, R. R., Kiel, M., and Eldering, A.: Towards sector-based attribution  
1117 using intra-city variations in satellite-based emission ratios between CO<sub>2</sub> and CO, *Atmos. Chem. Phys.*, 22, 14547-14570,  
1118 <https://doi.org/10.5194/acp-22-14547-2022>, 2022a.

1119 Wu, K., Davis, K. J., Miles, N. L., Richardson, S. J., Lauvaux, T., Sarmiento, D. P., Balashov, N. V., Keller, K., Turnbull, J.,  
1120 and Gurney, K. R.: Source decomposition of eddy-covariance CO<sub>2</sub> flux measurements for evaluating a high-resolution  
1121 urban CO<sub>2</sub> emissions inventory, *Environ. Res. Lett.*, 17, 074035, <https://doi.org/10.1088/1748-9326/ac7c29>, 2022b.

1122 Wu, M., Wu, D., Fan, Q., Wang, B. M., Li, H. W., and Fan, S. J.: Observational studies of the meteorological characteristics  
1123 associated with poor air quality over the Pearl River Delta in China, *Atmos. Chem. Phys.*, 13, 10755-10766,  
1124 <https://doi.org/10.5194/acp-13-10755-2013>, 2013.

1125 Xiao, Y., Yang, J., Cui, L., Deng, J., Fu, P., and Zhu, J.: Weakened Sea - Land Breeze in a Coastal Megacity Driven by  
1126 Urbanization and Ocean Warming, *Earth's Future*, 11, e2022EF003341, <https://doi.org/10.1029/2022EF003341>, 2023.

1127 Xu, R., Tong, D., Xiao, Q., Qin, X., Chen, C., Yan, L., Cheng, J., Cui, C., Hu, H., and Liu, W.: MEIC-global-CO<sub>2</sub>: A new  
1128 global CO<sub>2</sub> emission inventory with highly-resolved source category and sub-country information, *Sci. China Earth Sci*, 67,  
1129 450-465, <https://doi.org/10.1007/s11430-023-1230-3>, 2024.

1130 Xueref-Remy, I., Dieudonné, E., Vuillemin, C., Lopez, M., Lac, C., Schmidt, M., Delmotte, M., Chevallier, F., Ravetta, F.,  
1131 Perrussel, O., Ciais, P., Bréon, F.-M., Broquet, G., Ramonet, M., Spain, T. G., and Ampe, C.: Diurnal, synoptic and seasonal  
1132 variability of atmospheric CO<sub>2</sub> in the Paris megacity area, *Atmos. Chem. Phys.*, 18, 3335-3362, <https://doi.org/10.5194/acp-18-3335-2018>, 2018.

1134 Yadav, V., Ghosh, S., Mueller, K., Karion, A., Roest, G., Gourdji, S. M., Lopez - Coto, I., Gurney, K. R., Parazoo, N., and  
1135 Verhulst, K. R.: The impact of COVID - 19 on CO<sub>2</sub> emissions in the Los Angeles and Washington DC/Baltimore  
1136 metropolitan areas, *Geophys. Res. Lett.*, 48, e2021GL092744, <https://doi.org/10.1029/2021GL092744>, 2021.

1137 Yang, H., Wu, K., Shen, H., Janssens-Maenhout, G., Crippa, M., Guizzardi, D., and Zhou, M.: A comparative analysis of  
1138 China's anthropogenic CO<sub>2</sub> emissions (2000–2023): insights from six bottom-up inventories and uncertainty assessment,  
1139 *Atmos. Chem. Phys.*, 25, 18111-18127, <https://doi.org/10.5194/acp-25-18111-2025>, 2025.

1140 Yang, J. and Huang, X.: The 30 m annual land cover datasets and its dynamics in China from 1985 to 2024, *Earth System  
1141 Science Data [dataset]*, <https://doi.org/10.5281/zenodo.15853565>, 2025.

1142 Yang, T., Li, H. Y., Cao, J., Lu, Q. Q., Wang, Z. F., He, L. T., Sun, H. H., and Han, K.: Investigating the climatology of North  
1143 China's urban inland lake based on six years of observations, *Sci. Total Environ.*, 826,  
1144 <https://doi.org/10.1016/j.scitotenv.2022.154120>, 2022.

1145 Yang, Y., Zhou, M., Wang, T., Yao, B., Han, P., Ji, D., Zhou, W., Sun, Y., Wang, G., and Wang, P.: Spatial and temporal  
1146 variations of CO<sub>2</sub> mole fractions observed at Beijing, Xianghe, and Xinglong in North China, *Atmos. Chem. Phys.*, 21,  
1147 11741-11757, <https://doi.org/10.5194/acp-21-11741-2021>, 2021.

1148 Ye, X., Lauvaux, T., Kort, E. A., Oda, T., Feng, S., Lin, J. C., Yang, E. G., and Wu, D.: Constraining fossil fuel CO<sub>2</sub> emissions  
1149 from urban area using OCO - 2 observations of total column CO<sub>2</sub>, *J. Geophys. Res.-Atmos.*, 125, e2019JD030528,

1150 <https://doi.org/10.1029/2019JD030528>, 2020.

1151 You, C. and Chi-Hung Fung, J.: Characteristics of the Sea-Breeze Circulation in the Pearl River Delta Region and Its  
1152 Dynamical Diagnosis, *J. Appl. Meteorol. Clim.*, 58, 741-755, <https://doi.org/10.1175/jamc-d-18-0153.1>, 2019.

1153 Young, H. A., Turnbull, J. C., Keller, E. D., Domingues, L. G., Parry-Thompson, J., Hilton, T. W., Brailsford, G. W., Gray, S.,  
1154 Moss, R. C., and Mikaloff-Fletcher, S.: Urban flask measurements of CO<sub>2</sub>ff and CO to identify emission sources at different  
1155 site types in Auckland, New Zealand, *Philosophical Transactions of the Royal Society A*, 381, 20220204,  
1156 <https://doi.org/10.1098/rsta.2022.0204>, 2023.

1157 Zhang, L., Lin, J., Shao, Y., Huang, S., Fan, S., and Wei, W.: Understanding the impact of sea and land breezes on ozone  
1158 pollution in the Pearl River Delta, *Acta Scientiae Circumstantiae*, 44(1), 74-85, <https://doi.org/10.13671/j.hjkxxb.2023.0285>,  
1159 2024.

1160 Zhao, D., Xin, J., Wang, W., Jia, D., Wang, Z., Xiao, H., Liu, C., Zhou, J., Tong, L., and Ma, Y.: Effects of the sea-land breeze  
1161 on coastal ozone pollution in the Yangtze River Delta, China, *Sci. Total Environ.*, 807, 150306,  
1162 <https://doi.org/10.1016/j.scitotenv.2021.150306>, 2022.

1163 Zheng, B., Tong, D., Li, M., Liu, F., Hong, C., Geng, G., Li, H., Li, X., Peng, L., Qi, J., Yan, L., Zhang, Y., Zhao, H., Zheng,  
1164 Y., He, K., and Zhang, Q.: Trends in China's anthropogenic emissions since 2010 as the consequence of clean air actions,  
1165 *Atmos. Chem. Phys.*, 18, 14095-14111, <https://doi.org/10.5194/acp-18-14095-2018>, 2018.

1166 Zheng, Y., Jiang, F., Feng, S., Shen, Y., Liu, H., Guo, H., Lyu, X., Jia, M., and Lou, C.: Large-scale land-sea interactions extend  
1167 ozone pollution duration in coastal cities along northern China, *Env. Sci. Ecotechnol.*, 18, 100322,  
1168 <https://doi.org/10.1016/j.ese.2023.100322>, 2024.

1169